Flow Turbulence Combust
DOI 10.1007/s10494-011-9380-x

Turbulence Resolution Scale Dependence in Large-Eddy Simulations of a Jet Flame

Konstantin A. Kemenov · Haifeng Wang · Stephen B. Pope

Received: 20 April 2011 / Accepted: 8 November 2011

Abstract The explicit dependence of LES fields on the turbulence resolution scale Δ implies that LES statistics usually vary with Δ and exhibit different convergence behaviors for different types of statistics, flow variables and subgrid LES models. The present work compares the performance of two popular subgrid models—the dynamic Smagorinsky model and the Vreman model—based on the convergence of their LES statistics with respect to Δ for a piloted methane-air (Sandia D) flame. The Δ-dependence of the LES statistics is studied based on five grids with progressively increased resolution ranging from 3×10^5 to about 10.4×10^6 cells. The simulation results show that the resolved velocity statistics converge for the finest grids with some weak Δ-dependence observed in the variance fields. The mixture fraction statistics are found to be more sensitive to the turbulence resolution scale upstream in the flame signifying the importance of the estimation of the Δ-invariant LES statistics at the DNS limit. For the considered flame the Vreman subgrid model exhibits good performance with the statistics being very close to those given by the dynamic Smagorinsky model, and being rather insensitive to a choice of the model constant.

Keywords LES · Piloted diffusion flame · Subgrid-scale modeling · Turbulence resolution scale

1 Introduction

Large-eddy simulation (LES) of turbulent combustion flows is challenging because some important rate-controlling processes are acting at the small-scales that are out of reach for a typical LES grid in computationally feasible simulations [1]. The effects

K. A. Kemenov (✉) · H. Wang · S. B. Pope
Sibley School of Mechanical and Aerospace Engineering, Cornell University, Ithaca, NY 14853, USA
e-mail: kak262@cornell.edu

of these unresolved processes that are strongly coupled to the unresolved turbulent motions require modeling. Accounting for these effects on the large (resolved) scales of the turbulent motion results in the appearance of the subgrid scale (SGS) modeling terms which presumably regularize the original governing (Navier-Stokes) equations [2], and leads to the LES governing equations for the resolved flow at some turbulent resolution scale Δ. In the traditional interpretation of LES as a filtering approach, and which we do not take in the present work, Δ is viewed as the characteristic filter width.

The practical importance of the LES methodology as a prospective engineering tool for combustion devices has been well appreciated and demonstrated in growing numbers of research simulations of real-life combustor geometries [3–7]. Among the most important issues that need to be addressed as LES matures as an effective predictive tool for complex engineering flows is the quality assessment and quantification of uncertainty of the LES solution [8].

It has been widely recognized that in LES the discrete solution at a particular turbulent resolution scale Δ is affected by the grid resolution h, the numerical discretization scheme and the adopted SGS models. In practical LES the turbulent resolution scale Δ is typically associated with the grid resolution, i.e., $\Delta = h$, as there is a need for the better resolution of the turbulent motion and its interaction with physical processes of interest. On the other hand, this might lead to the significant effects of the numerical errors on the discrete LES solution [9, 10]. The non-trivial interactions between the numerical and SGS modeling errors make it difficult to separate them and, as a result, to unambiguously assess the quality of the SGS models. In [11] Meyers et al. introduced a computational "error-landscape" procedure to study the combined simulation error by systematically varying both the grid resolution and the modeling (Smagorinsky) constant and comparing the LES based global measure, such as the spatially averaged resolved kinetic energy, with the reference explicitly filtered DNS counterpart for a case LES of decaying isotropic turbulence with the Smagorinsky SGS model. It was demonstrated that such a defined simulation error resembles a "valley"-shaped surface (landscape) when it is viewed as a function of the grid resolution and the Smagorinsky constant. The existence of the valley region suggests an optimal functional relationship between the Smagorinsky constant and the grid resolution which minimizes the adopted simulation error measure and allows one to qualitatively assess the effect of different discretization schemes [12, 13].

In practically relevant LES studies, however, (1) the reference flow data obtained with a help of the DNS or high-resolution experiments are usually not available, (2) there is an ambiguity in identifying a suitable global variable to define the error measure due to inhomogeneity of flow and usage of non-uniform grids, and (3) systematic grid dependency studies are typically not viable due to significant computing expenses. In addition, it is remarked here that a procedure of comparison of the LES solution with the filtered DNS solution represents a highly questionable practice due to several reasons [14, 15], among others are the fact that the filtered DNS realization does not constitute a solution of the LES equations and the lack of ability to represent a distribution of DNS fields corresponding to a given LES solution. Furthermore, it should be appreciated that an ultimate objective of LES is not obtaining the LES solution (statistics) at a particular resolution scale Δ, but producing a reliable estimate for the statistics of the total (unfiltered) DNS flow field of interest [14]. Even if a particular LES model could lead to the solution that is arbitrarily close to the corresponding filtered DNS solution (in a statistical sense) it still can be an inadequate estimate for the statistics of the full flow field, especially in the light of using rather coarse LES grids.

Other attempts to formulate a general error estimating approach for LES that involve several LES calculations include the grid/model variation approach of Klein [16] and the LES quality index approach of Celik et al. [17]. Essentially, both approaches center on the assumption that the residual fields can be taken equal to an additive sum of exponential terms, i.e., $a_n\Delta^n + a_m\Delta^m$, which represent the contributions from the discretization and modeling errors, respectively. Then, it is formally possible to obtain the unknown model coefficients and exponents from a number of LES calculations employing grids with different resolutions [8]. A number of less computationally intensive approaches recently proposed in the literature and characterized by a single LES calculation have been recently reviewed by Gant [18], and they are not the focus of the present work. In this paper, we are primarily concerned with the Δ-dependence of the LES statistics and its sensitivity to different SGS models along with the approach introduced by Pope in [14].

At the continuous level the resolved LES solution is a function of the turbulence resolution length scale $\Delta(\boldsymbol{x})$ because of its explicit appearance in the modeled subgrid-scale terms. In the DNS limit, when $\Delta/\mathcal{L} \to 0$ for some characteristic length $\mathcal{L}$, the LES solution tends to the DNS solution as the subgrid-scale terms vanish. Further discretization and numerical integration of the LES equations introduce additional dependence on Δ through the dependence on sizes of an LES grid cell with respect to the corresponding coordinate directions, i.e., $(\Delta x_1, \Delta x_2, \Delta x_3)$. In practical LES, the characteristic length scale of an LES cell $h = h(\Delta x_1, \Delta x_2, \Delta x_3)$ is usually specified (for example, as a grid cell volume) and associated with $\Delta = h$. The different specifications of $\Delta(\boldsymbol{x})$ lead to the different LES governing equations resulting in presumably different LES solutions. In addition, the discrete approximations of these LES solutions are subject to a complex interplay among various types of errors defined by a choice of the discretization scheme (numerical errors), SGS models (modeling errors) and LES grids (numerical and modeling errors). Therefore, it is practically relevant to study the LES models under the influence of the overall simulation error.

In this paper, we view the LES solution, say for example the mixture fraction field $\tilde{\xi}(\boldsymbol{x}, t)$, as a class of functions $\{\tilde{\xi}_\Delta\}$ parametrized by $\Delta(\boldsymbol{x})$ and represented as a collection of LES fields $\{\tilde{\xi}_\Delta\} = \{\dots, \tilde{\xi}_{\Delta_1}, \tilde{\xi}_{\Delta_2}, \tilde{\xi}_{\Delta_3}, \dots\}$ with respect to monotonically decreasing sequence of the turbulent resolution scales $\{\dots > \Delta_1 > \Delta_2 > \Delta_3 > \dots\}$. The LES class $\{\tilde{\xi}_\Delta\}$ has a limiting point $\xi_\circ$ given by the DNS solution when $\Delta_i/\mathcal{L} \to 0$. The limiting point $\xi_\circ$ is rarely available or computationally prohibitive to obtain even for modest Re-number flows and simple geometries. Moreover, due to enormous computational cost such a class is never fully known, and as it is customarily done in practice a practitioner usually deals with one or two members from the LES class. A potential pitfall of such an approach is that knowing one or two members of the LES class might not be sufficient to unambiguously characterize the flow physics of a problem in hand [14]. Analogously, the corresponding class of the residual mixture fraction fields $\{\xi''_\Delta\} = \{\dots, \xi''_{\Delta_1}, \xi''_{\Delta_2}, \xi''_{\Delta_3}, \dots\}$ can be defined such that $\xi''_{\Delta_i} = \xi_\circ - \tilde{\xi}_{\Delta_i}$. Note that the present point of view on the LES solution is conceptually different from the explicit filtering LES approach that aims to produce the grid-independent

LES solution for the particular SGS model and filter by separating the modeling and numerical errors [19].

Because of the random character of LES it is appropriate to assess the LES solution based on the LES derived statistics. For example, if the statistical mean of the LES solution $\{\tilde{\xi}_\Delta\}$ is the statistic of interest then the corresponding LES statistic is represented by $Q^W(\Delta) = \{\ldots, \langle\tilde{\xi}_{\Delta_1}\rangle, \langle\tilde{\xi}_{\Delta_2}\rangle, \langle\tilde{\xi}_{\Delta_3}\rangle, \ldots\}$ with a limiting point $Q = \langle\xi_\circ\rangle$ denoting the true mean of the DNS solution. Similarly, the residual based statistic is then defined as $Q^r(\Delta) = Q - Q^W(\Delta) = \{\ldots, \langle\xi''_{\Delta_1}\rangle, \langle\xi''_{\Delta_2}\rangle, \langle\xi''_{\Delta_3}\rangle, \ldots\}$. The practical objective of LES is to produce accurate estimates $Q^m(\Delta) = Q^W(\Delta) + Q^r(\Delta)$ for the true statistics Q, i.e., $Q^m(\Delta) \approx Q$. Then, the predictive capabilities of a particular LES are assessed based on how close the total LES statistics $Q^m(\Delta)$ approximate the true DNS statistics Q as well as how fast $Q^m(\Delta)$ converges to Q with respect to Δ [14].

Thus, our error-assessment LES procedure includes the following components:

(a) A model specification for the residual statistics Q^r;
(b) An estimation of the total LES statistics for several turbulence resolution scales (grids) Δ_i, $Q^m(\Delta) = Q^W(\Delta) + Q^r(\Delta)$, and an identification of possible convergence of the statistics with respect to Δ;
(c) An assessment of the overall simulation error $\epsilon(\Delta) = Q - Q^m(\Delta)$ as a function of Δ, if the true statistics Q $(Q \equiv Q^W(0))$ are available from DNS. Note that employing the experimental statistics Q_e, say from the high-resolution experiments, as Q could introduce extra sources of errors due to (i) the inherited uncertainties in the measurements on one hand, and (ii) the simplified treatment (physical modeling errors) of combustion and molecular diffusion processes on the other, i.e., $Q \neq Q_\mathrm{e}$;
(d) Generally, since the true statistics Q are not available a procedure to estimate Q is required based on the fact that $Q^m(\Delta) \to Q$ (i.e., $(Q^m(\Delta) - Q^W(\Delta)) \to 0$) if $Q^r(\Delta) \to 0$ as $\Delta \to 0$. In this case, an LES model is deemed to be *consistent* at the DNS limit. This is not always the case, however, and it could be that $Q^r(\Delta) \neq 0$ as $\Delta \to 0$. Clearly, the DNS limit consistency is a desirable property for an LES model.

The present work focuses on items (a), (b) and partially on (c). Item (d) is the most challenging to address and requires a model for $Q^m = Q^m(\Delta)$ for the turbulence resolution length scales that are smaller than those employed in LES calculations, i.e., $\Delta < \Delta_i$. Other computationally important questions are how to choose Δ_i optimally, i.e., as large are possible, and how many Δ_i (thus, a number of LES calculations) are sufficient to accurately describe the functional dependence of $Q^m(\Delta)$. These issues are also left out of scope of the the present paper.

The present approach allows one to compare SGS models based on how they affect the total LES statistics with respect to Δ. These type of studies which focus on the turbulence resolution effects on the statistics of LES solution are still rare in the combustion LES literature [7, 20]. The present study, therefore, aims to fill this gap partially by examining the performance of two popular SGS models—the dynamic Smagorinsky SGS model [21] and the Vreman SGS model [22], for a case of the non-premixed methane-air jet flame (Sandia flame D). This piloted flame has been extensively studied experimentally [23, 24] and computationally [25–32].

2 Governing Equations

2.1 LES equations

A common way to reduce the complex combustion chemistry in LES of non-premixed flames is the mixture fraction based flamelet approach [33, 34], which we follow in this paper. In the flamelet approach chemical composition, temperature and density are parameterized by one (or a few) variables such as the mixture fraction and its scalar dissipation rate, or a progress variable which is usually constructed as a linear combination of specially chosen chemical species [35].

In the present work, we employ a single mildly-strained steady laminar flamelet where thermochemical variables and density depend on the mixture fraction only and are represented by non-linear functional relationships. In variable-density LES the Δ-resolved quantities, i.e. density $\bar{\rho}(\Delta)$, velocity $\tilde{u}_i(\Delta)$ and mixture fraction fields $\tilde{\xi}(\Delta)$, are of importance. Here, the common Favre notation for the density-weighted resolved quantity is adopted, i.e., $\tilde{\xi}(\Delta) = \overline{\rho\xi}(\Delta)/\bar{\rho}(\Delta)$ and the bar symbol stands for the resolved (filtered) quantities. Because of the non-linear flamelet parametrization the resolved density and thermochemical quantities require accounting for the small-scale (unresolved) mixture fraction fluctuations which is achieved through dependence on the SGS mixture fraction variance $V_\xi(\Delta) \equiv \widetilde{\xi^2}(\Delta) - (\tilde{\xi}(\Delta))^2$ [36].

Thus, the LES system of the governing equations for the resolved density, velocity, mixture fraction and the SGS mixture fraction variance takes the following form:

$$\frac{\partial \bar{\rho}}{\partial t} + \frac{\partial \bar{\rho}\tilde{u}_j}{\partial x_j} = 0, \tag{1}$$

$$\frac{\partial \bar{\rho}\tilde{u}_i}{\partial t} + \frac{\partial \bar{\rho}\tilde{u}_i\tilde{u}_j}{\partial x_j} = -\frac{\partial \bar{p}}{\partial x_i} + 2\frac{\partial}{\partial x_j}\left((\bar{\mu} + \mu_T)\left(\widetilde{S}_{ij} - \frac{1}{3}\widetilde{S}_{kk}\delta_{ij}\right)\right), \tag{2}$$

$$\frac{\partial \bar{\rho}\tilde{\xi}}{\partial t} + \frac{\partial \bar{\rho}\tilde{u}_j\tilde{\xi}}{\partial x_j} = \frac{\partial}{\partial x_j}\left(\bar{\rho}\left(\widetilde{\mathcal{D}} + \mathcal{D}_T\right)\frac{\partial \tilde{\xi}}{\partial x_j}\right), \tag{3}$$

$$\frac{\partial \bar{\rho}V_\xi}{\partial t} + \frac{\partial \bar{\rho}\tilde{u}_j V_\xi}{\partial x_j} = \frac{\partial}{\partial x_j}\left(\bar{\rho}\left(\widetilde{\mathcal{D}} + \mathcal{D}_T\right)\frac{\partial V_\xi}{\partial x_j}\right) - 2\bar{\rho}\widetilde{\chi}_\xi + 2\bar{\rho}\left(\widetilde{\mathcal{D}} + \mathcal{D}_T\right)\left(\frac{\partial \tilde{\xi}}{\partial x_j}\right)^2 \tag{4}$$

Here, $\bar{p}$, $\widetilde{S}_{ij}$ and $\widetilde{\chi}_\xi$ are the resolved pressure, strain rate and scalar dissipation rate, respectively. The scalar dissipation rate is decomposed into the resolved and SGS parts and is modeled in a standard way as [29, 37]:

$$2\overline{\rho\mathcal{D}|\nabla\xi|^2} = 2\bar{\rho}\widetilde{\chi}_\xi = 2\bar{\rho}\widetilde{\mathcal{D}}\frac{\partial \tilde{\xi}}{\partial x_j}\frac{\partial \tilde{\xi}}{\partial x_j} + C\frac{\bar{\rho}\mathcal{D}_T V_\xi}{\Delta^2}, \tag{5}$$

where C is a model constant chosen to be $C = 2$ [32]. The closure of the subgrid terms is based on the subgrid eddy viscosity $\mu_T(\Delta)$ as detailed in Section 2.2. The subgrid diffusivity $\bar{\rho}D_T(\Delta)$ is specified based on the eddy viscosity and the subgrid Schmidt number $\bar{\rho}D_T = \mu_T/Sc_T$, with a commonly used value of $Sc_T = 0.4$ [25]. Finally, to close the system of Eqs. 1–4 the flamelet model equations ($\bar{\rho} = \bar{\rho}(\tilde{\xi}, V_\xi)$, $\widetilde{T} = \widetilde{T}(\tilde{\xi}, V_\xi)$) and molecular transport properties ($\bar{\mu} = \overline{\mu(T)}$, $\bar{\rho}\widetilde{\mathcal{D}} = \bar{\rho}\widetilde{\mathcal{D}(T)}$) are specified in Section 2.3.

2.2 SGS models

In this section we describe the subgrid scale models needed to relate the unknown subgrid stresses and fluxes to the known resolved quantities.

In both scalar equations, Eqs. 3 and 4, the unclosed subgrid scalar fluxes are modeled by a standard gradient diffusion hypothesis with the same subgrid diffusivity $\bar{\rho}\mathcal{D}_T$ for both $\tilde{\xi}$ and $\widetilde{\xi^2}$ fields:

$$(\bar{\rho}\widetilde{u}_j\tilde{\xi} - \bar{\rho}\widetilde{u_j\xi}) = \bar{\rho}\mathcal{D}_T\frac{\partial\tilde{\xi}}{\partial x_j}, \tag{6}$$

$$(\bar{\rho}\widetilde{u}_j\widetilde{\xi^2} - \bar{\rho}\widetilde{u_j\xi^2}) - 2\tilde{\xi}(\bar{\rho}\widetilde{u}_j\tilde{\xi} - \bar{\rho}\widetilde{u_j\xi}) = \bar{\rho}\mathcal{D}_T\frac{\partial V_\xi}{\partial x_j}. \tag{7}$$

In this paper, we study the SGS stress models that are based on the eddy-viscosity assumption. Accordingly, the deviatoric part of the unclosed SGS stress $\tau_{ij} = \bar{\rho}\tilde{u}_i\tilde{u}_j - \bar{\rho}\widetilde{u_i u_j}$ in the LES momentum equation, Eq. 2, is modeled as

$$\tau_{ij} - \delta_{ij}\tau_{kk}/3 = 2\mu_T(\widetilde{S}_{ij} - \delta_{ij}\widetilde{S}_{kk}/3), \tag{8}$$

where μ_T is the SGS eddy viscosity. The first SGS model considered is the standard dynamic Smagorinsky (DSMG) model with μ_T taken to be:

$$\mu_T = \bar{\rho}C_\mu\Delta^2(2\widetilde{S}_{ij}\widetilde{S}_{ij})^{1/2}, \tag{9}$$

Here, μ_T involves a model constant C_μ which is computed according to the Germano dynamic procedure [21] with Lilly's modification [38]. In addition, a commonly used averaging operation in the periodic homogeneous direction is employed for the numerator and denominator in the expression for C_μ.

The second SGS model considered in the paper is the recently proposed eddy-viscosity model due to Vreman [22] which is given by

$$\mu_T = \bar{\rho}C_v\sqrt{\frac{B_\beta}{\alpha_{ml}\alpha_{ml}}}, \quad \alpha_{ml} = \frac{\partial\widetilde{u}_l}{\partial x_m}, \tag{10}$$

with B_β being the second invariant of a tensor quantity β_{ij} defined as

$$\beta_{ij} = \Delta_m^2\alpha_{mi}\alpha_{mj}, \quad B_\beta = \beta_{11}\beta_{22} + \beta_{22}\beta_{33} + \beta_{11}\beta_{33} - \beta_{12}^2 - \beta_{23}^2 - \beta_{13}^2, \tag{11}$$

where Δ_m is the resolution scale in the x_m coordinate direction. The model constant C_v can be related to the Smagorinsky constant $C_v = 2.5C_S^2$ for the case of homogeneous and isotropic turbulence ($C_S = 0.17$) [22].

The Vreman SGS model has been constructed to produce the vanishing SGS dissipation for a quite wide class of laminar shear flows and to be fully realizable. It does not require any ad-hoc procedures such as clipping, averaging or explicit filtering. The model has demonstrated encouraging results not only for simple wall-bounded and transitional shear flows [22], but also for complex respiratory flows (with $C_S = 0.065$) [39] and turbulent diffusion flames (with $C_S = 0.1$) [30]. Non-universality of the model constant C_v has been recognized by Park et al. [40] who proposed a procedure for evaluating the global model constant based on the Germano dynamic approach.

In this paper, we consider the Vreman SGS model with two values of the constant C_v: a standard value of $C_v = 0.025$ (Vreman-I) which corresponds to $C_S = 0.1$, and twice this value, i.e., $C_v = 0.05$ (Vreman-II). Note that for the latter case (Vreman-II) the modeling constant C in Eq. 5 needs to be halved to guarantee the same SGS dissipation rate s_χ in Eq. 4 for both cases, as dictated by:

$$s_\chi = C\frac{\mu_T V_\xi}{Sc_T\Delta^2} = CC_v\frac{\bar{\rho}V_\xi}{Sc_T\Delta^2}\sqrt{\frac{B_\beta}{\alpha_{ml}\alpha_{ml}}} \quad (12)$$

Thus, for Vreman-II model, we set C_v and C to be equal to 0.05 and 1.0, respectively.

2.3 Combustion model

The specification of the combustion model equations and transport properties follows closely to that of [32]. Here, we briefly summarize the main assumptions and resulting equations.

The functional relationships between the mixture fraction on the one hand and density and thermochemical variables on the other, are obtained from a steady laminar flamelet solution using CHEMKIN 4.1. A mildly-strained flamelet solution with a nominal strain rate of $a = 50\ \mathrm{s}^{-1}$ is computed in a 1D counter-flow configuration using the detailed GRI-Mech 3.0 chemical mechanism. The flamelet solutions obtained are then approximated by quadratic B-spline functions. For example, the specific volume $v(\xi) = \rho^{-1}(\xi)$ is represented by a quadratic B-spline $v_s(\xi)$. In its simplest form a quadratic B-spline approximation is represented by a single quadratic function $v_o(\xi) = a + b\xi + c\xi^2$ with the specified constant coefficients a, b and c obtained from fitting to the CHEMKIN flamelet data. Note that this single quadratic representation allows to express the resolved specific volume directly (without introducing an assumed PDF) as:

$$\widetilde{v}_o(\tilde{\xi}, V_\xi) = a + b\tilde{\xi} + c\widetilde{\xi^2} = a + b\tilde{\xi} + c(\tilde{\xi}^2 + V_\xi) = \widetilde{v}_o(\tilde{\xi}, 0) + cV_\xi, \quad (13)$$

with $\widetilde{v}_o(\tilde{\xi}, 0) = v_o(\tilde{\xi})$. However, as it is evident from Fig. 1 a single quadratic function gives a rather crude approximation of the flamelet profile overpredicting the specific volume (i.e., underpredicting density) for rich mixtures. Clearly, the spline approximation $v_s(\xi)$ can be made arbitrarily close to the flamelet solution by considering a general piece-wise quadratic approximation based on quadratic B-splines written as:

$$v_s(\xi) = \sum_{i=1}^{n} c_i B_{i,2}(\xi). \quad (14)$$

Here, $\{B_{i,2}\}_{i=1}^n$ are quadratic B-splines and $(c_i)_{i=1}^n$ is a set of control points. The j-th B-spline of degree $d = 2$ (quadratic), $B_{j,d}(\xi)$, is fully defined by its knots sequence $(\xi_j)_{j=1}^{n+d+1}$ as:

$$B_{j,d}(\xi) = \frac{\xi - \xi_j}{\xi_{j+d} - \xi_j}B_{j,d-1}(\xi) + \frac{\xi_{j+1+d} - \xi}{\xi_{j+d+1} - \xi_{j+1}}B_{j+1,d-1}, \quad (15)$$

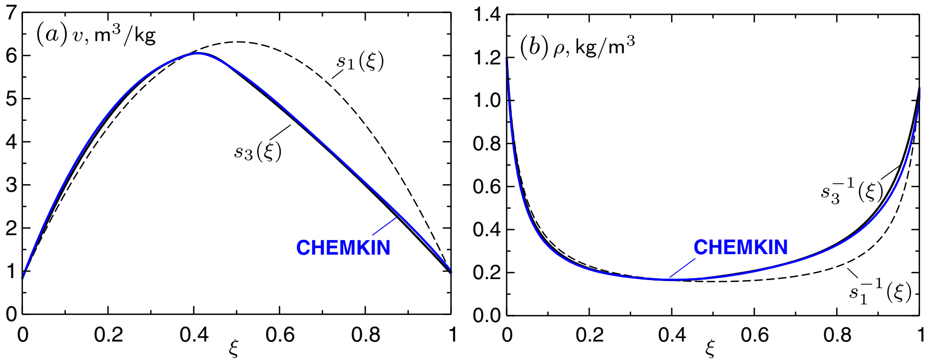

Fig. 1 Specific volume (**a**) and density (**b**) vs. mixture fraction for the CHEMKIN flamelet solutions and quadratic B-spline approximations $s_1(\xi)$ and $s_3(\xi)$ employing 1 and 3 parabolic pieces, respectively. The quadratic B-spline approximation $s_3(\xi)$ is defined by the control points $(c_i)_{i=1}^5 = (0.834, 5.543, 6.131, 3.801, 0.947)$ and the knot sequence $(\xi_j)_{j=1}^8 = (0, 0, 0, 0.39, 0.474, 1, 1, 1)$

with

$$B_{j,0}(\xi) = \begin{cases} 1, \text{ if } \xi_j \leq \xi < \xi_{j+1} \\ 0, \text{ otherwise.} \end{cases} \tag{16}$$

In this work, to approximate the flamelet solutions, we consider quadratic B-spline approximations consisting of three parabolic pieces ($n = 5$) as shown in Fig. 1 for the specific volume. This figure also shows the corresponding knot sequence $(\xi_j)_{j=1}^8$ and control points $(c_i)_{i=1}^5$ used to define the piece-wise quadratic B-spline approximations $v_s(\xi)$. Once the approximation for the flamelet solution is available, we define the resolved specific volume $\widetilde{v}(\tilde{\xi}, V_\xi)$ (and therefore the resolved density $\bar{\rho} = \widetilde{v}^{-1}$) as:

$$\widetilde{v}(\tilde{\xi}, V_\xi) = v_s(\tilde{\xi}) \frac{\widetilde{v}_o(\tilde{\xi}, V_\xi)}{\widetilde{v}_o(\tilde{\xi}, 0)}. \tag{17}$$

This model is equivalent to the following relations

$$\widetilde{v}(\tilde{\xi}, 0) = v_s(\tilde{\xi}), \quad \frac{\widetilde{v}(\tilde{\xi}, V_\xi)}{\widetilde{v}(\tilde{\xi}, 0)} = \frac{\widetilde{v}_o(\tilde{\xi}, V_\xi)}{\widetilde{v}_o(\tilde{\xi}, 0)}, \tag{18}$$

and indeed these relations are the motivation for the model. They show that in the absence of the subgrid fluctuations the resolved specific volume coincides with the flamelet approximation. On the other hand, when the subgrid fluctuations are present (non-zero variance) the change of the resolved specific volume with respect to the zero variance state is equal to the same change computed based on single quadratic approximation. Note that $\widetilde{v}(\tilde{\xi}, V_\xi)$ is known in terms of $\tilde{\xi}$, V_ξ and the approximated flamelet profile $v_s(\tilde{\xi})$, whereas the exact values of $\widetilde{v}$ depends on the PDF of the mixture fraction, not solely on its first moments. Similar expressions can be applied to other thermochemical variables [32]. An advantage of the present approach is that it allows to completely exclude the flamelet table look-up procedure and, as a result, associated with it interpolation errors, while a disadvantage being that a PDF corresponding to Eq. 17 is not explicitly known and surely not unique.

The functional dependences of the mixture molecular viscosity and mixture fraction diffusivity on temperature are also computed from CHEMKIN and are represented in a power-law form given by:

$$\mu(T) = 1.75 \times 10^{-5}\left(\frac{T}{T_0}\right)^{0.69} \frac{\mathrm{kg}}{\mathrm{m}\cdot\mathrm{s}}, \quad \rho D(T) = 2.48 \times 10^{-5}\left(\frac{T}{T_0}\right)^{0.72} \frac{\mathrm{kg}}{\mathrm{m}\cdot\mathrm{s}}, \tag{19}$$

with $T_0 = 298$ K. Thus, the molecular Schmidt $Sc = \bar{\mu}/\bar{\rho}\widetilde{D}$ number shows only a mild dependence on temperature and is equal to 0.7, approximately.

3 Computational Setup

3.1 Sandia flame D

Sandia flame D has been extensively studied in the experimental works of Barlow and Frank [23] and Schneider et al. [24]. This piloted flame is characterized by a minimal level of local extinction due to moderate strain rates exerted by the velocity field, and therefore, is assessable for studies using relatively simple combustion models.

The fuel jet consists of a mixture of 25% methane and 75% air (by volume) and emanates from a nozzle with diameter $D = 7.2$ mm at a bulk velocity of $U_b = 49.6$ m/s and temperature of 294 K. The nozzle is surrounded by a coaxial pilot nozzle with diameter of 2.62D. The hot pilot flow is a lean burnt mixture of C_2H_2, air, CO_2, H_2 and N_2 corresponding to a mixture fraction value of $\xi = 0.271$, with a bulk velocity of 11.4 m/s and temperature of 1,880 K. The coaxial burner is further surrounded by co-flowing air with a bulk velocity of 0.9 m/s and temperature of 291 K. A characteristic Reynolds number of $Re = 22{,}400$ is determined based on the fuel jet velocity, kinematic viscosity ($\nu = 1.58 \times 10^{-5}\mathrm{m}^2/\mathrm{s}$) and the nozzle diameter.

3.2 Numerical discretization and modeling

A version of the structured Stanford LES code [35] with the modified discretization of the momentum convective terms due to Wang and Caughey (manuscript in preparation) is employed to solve the variable-density LES equations written in cylindrical coordinates (x, r, θ). The numerical method is second-order accurate in space and time. For the momentum equation, it adopts a discretization scheme which is energy-conserving on uniform grids. Scalar transport equations are discretized using the QUICK scheme [41] and solved employing a semi-implicit iterative technique, which has proven to be effective for typical low-Mach combustion problems [29, 35]. Domain decomposition is used for the LES code parallelization.

In this work, we perform the flow simulations in a cylindrical computational domain of extent $100.3D \times 20D \times 2\pi$. The jet and pilot nozzles have a small axial extension of $0.3D$ upstream of the nozzle exit plane, which is taken as the origin of the axial coordinate, x. The dimensions of the computational domain as well as flow variables are non-dimensionalized by the characteristic jet parameters (i.e., diameter, bulk velocity, density).

The jet inflow boundary condition for velocity is generated separately [29] by running a high resolution LES of the incompressible stationary turbulent pipe

Table 1 Grid resolutions, the minimum/maximum cell width, and the maximum (s_x^{max}, s_r^{max}) and averaged ($\langle s_x \rangle$, $\langle s_r \rangle$) cell stretch parameters in the non-dimensionalized axial and radial directions $\hat{x} \equiv x/D$, $\hat{r} \equiv r/D$

Grid	Resolution ($\hat{x}, \hat{r}, \theta$)	Δ_x^{min}	Δ_x^{max}	Δ_r^{min}	Δ_r^{max}	stretch, (%) s_x^{max}, $\langle s_x \rangle$	stretch, (%) s_r^{max}, $\langle s_r \rangle$
M_1	$108 \times 72 \times 40$	$10. \times 10^{-2}$	3.93	2.3×10^{-2}	1.52	4.2, 3.5	11, 9.8
M_2	$144 \times 96 \times 48$	7.5×10^{-2}	2.89	1.7×10^{-2}	1.27	3.0, 2.6	9.5, 8.8
M_3	$180 \times 120 \times 60$	6.0×10^{-2}	2.30	1.6×10^{-2}	1.03	2.4, 2.0	7.4, 5.7
M_4	$216 \times 156 \times 80$	5.0×10^{-2}	1.92	1.2×10^{-2}	0.80	2.0, 1.7	6.2, 4.7
M_5	$360 \times 240 \times 120$	3.0×10^{-2}	1.19	6.8×10^{-3}	0.53	1.3, 1.0	4.6, 3.3

flow where the experimental mean and rms axial velocity profiles as measured by Schneider et al. [24] are enforced. An LES of the turbulent pipe flow has been conducted on a $192 \times 96 \times 96$ grid with periodic boundary conditions in the streamwise direction. Accumulated velocity field data are saved in a database and used to generate inflow conditions by linear interpolation of a 2D cross-sectional slice onto the coarser LES grids at the jet inlet plane for the flame simulations. The inflow velocity condition for the pilot is based on the measured mean velocity with the superimposed uncorrelated random noise fluctuations of low intensity ($\sim 1\%$) according to the measured rms profiles, while in the co-flow region the measured bulk values with zero turbulent intensity are used. The mixture fraction field is prescribed as a step function according to an experimental value of $\tilde{\xi} = 0.271$ for the pilot, and $\tilde{\xi} = 1$ and $\tilde{\xi} = 0$ for the jet and co-flow, respectively. Finally, the convective boundary conditions are employed for velocity and scalar fields on the outflow boundary including the entrainment boundary of the computational domain.

To study the dependence of the LES statistics on the turbulence resolution scale Δ we employ five grids $M_1, \ldots, M_5$ with progressively increasing resolution from about 0.3 to 10.4 million cells as detailed in Table 1. All grids are non-uniformly stretched in the axial direction as well as in the radial direction, with clustering in the jet nozzle and pilot annulus regions, while remaining uniformly spaced in the circumferential direction. Grid resolution parameters for the jet nozzle and the pilot are given in Table 2.

In this paper, we consider a case when the turbulence resolution scale Δ is equal to the local numerical grid spacing measure $h(\boldsymbol{x})$, i.e., $h(\boldsymbol{x})/\Delta(\boldsymbol{x}) = 1$. We define the grid spacing measure, and therefore Δ, based on the differential length of a curve segment associated with an LES grid cell $\Delta(\boldsymbol{x}) = (\Delta_x^2 + \Delta_r^2 + (r\Delta_\theta)^2)^{1/2}$ rather than on the more traditional definition which is based on a volume of an LES grid cell, i.e.,

Table 2 Grid resolutions details for the jet nozzle and the pilot

Grid	Cells in $\hat{x}$ for $\hat{x} < 0$	Cells in $\hat{r}$ for jet nozzle	Cells in $\hat{r}$ for pilot	Cells in jet nozzle wall	Cells in pilot wall	Cells in $\hat{r}$ total
M_1	3	10	17	1	2	72
M_2	4	14	25	2	3	96
M_3	5	18	30	2	3	120
M_4	7	23	39	3	4	156
M_5	10	35	60	5	7	240

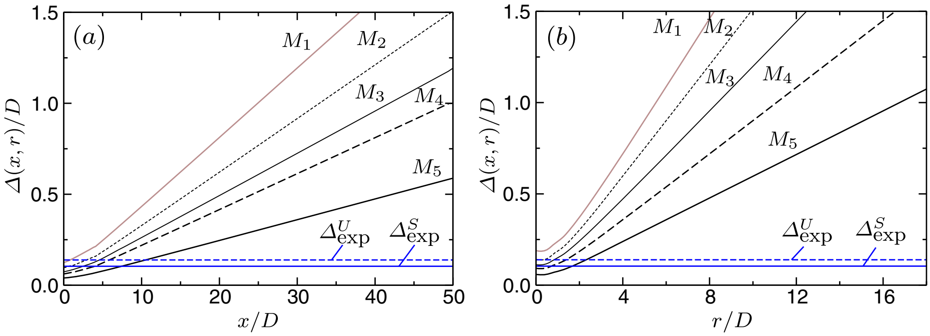

Fig. 2 Dependence of the non-dimensionalized turbulence resolution scales Δ_{M_i} with respect to (**a**) the axial coordinate direction at the centerline, and (**b**) the radial coordinate direction at an axial location of $x = 3D$. The non-dimensionalized spatial resolutions of the experimental measurements for scalar ($\Delta^S_{\text{exp}} = 0.104D$ [23]) and velocity ($\Delta^U_{\text{exp}} = 0.139D$ [24]) fields are shown by horizontal lines

$\Delta(\boldsymbol{x}) = (\Delta_x \Delta_r r \Delta_\theta)^{1/3}$. Here, Δ_x, Δ_r and Δ_θ denote grid spacings in the corresponding coordinate directions. Such an adopted definition of the turbulence resolution scale avoids the vanishing values of Δ on the jet centerline, or in cases where the grid resolution in a particular coordinate direction becomes very small (DNS-like). It is further remarked that the grids $\{M_1, \ldots, M_5\}$ are "monotonic" with respect to Δ. In other words, for every spatial point of the computational domain the following is true: $\Delta_{M_5} < \Delta_{M_4} < \Delta_{M_3} < \Delta_{M_2} < \Delta_{M_1}$, i.e., a particular grid M_i resolves more than the preceding grid M_{i-1} does. Figure 2 illustrates the dependence of $\Delta(x, r)$ on the radial coordinate at $x = 3D$ and on the axial coordinate at the centerline for all five grids. The experimental spatial resolutions for velocity and scalar fields [23, 24], Δ^U_{exp} and Δ^S_{exp}, are also shown by horizontal lines for comparison. It is seen that in the small near-field region ($x \lesssim 5D$ and $r \lesssim 1.5D$) almost all grids, except the coarsest M_1, provide resolutions comparable with the experimental ones, or even better. For example, the finest grid M_5 achieves better resolution than that of the experiments up to the distances of $x = 8D$ and $r = 2D$ in the axial and radial directions, respectively.

In all simulations, with an exception of the finest grid M_5, a zero state is employed as the initial condition for all scalar variables except the axial velocity field, which is taken to be uniform and equal to the co-flow velocity in the whole domain. For the finest grid, the initial fields are interpolated from a statistically-stationary solution on the preceding grid M_4. Time integration is performed with a variable time step corresponding to a CFL number of 0.18–0.36.

3.3 Estimation of the LES statistics

The LES based estimation of the total statistic Q can be represented as a sum of two components $Q^m(\Delta) = Q^W(\Delta) + Q^r(\Delta)$, where $Q^W(\Delta)$) is defined solely by the resolved LES fields, while $Q^r(\Delta)$ estimates the contribution from the residual fields [14]. In case of the statistical mean, for example the mean mixture fraction $Q \equiv \langle \xi \rangle = \langle \tilde{\xi} \rangle + \langle \xi'' \rangle$, the residual contribution is $\langle \xi'' \rangle$ can usually be neglected in free-shear flows and if the LES grid provides an adequate resolution, say $\Delta < \Delta^*_M$.

Here, the appropriate averaging is denoted by angular brackets. This gives the following estimation for the mean quantities:

$$Q \approx Q^m(\Delta) = Q^W(\Delta) + Q^r(\Delta) = \langle\tilde{\xi}\rangle + 0 = \langle\tilde{\xi}\rangle, \tag{20}$$

in other words $Q^W \equiv \langle\tilde{\xi}\rangle$ and $Q^r \equiv \langle\xi''\rangle = 0$.

In case of the variance $Q \equiv \langle\xi^2\rangle - \langle\xi\rangle^2$, the residual contribution is important and has to be accounted for. The most general decomposition of the scalar variance into the resolved and residual components was recently proposed and studied by Vervisch et al. [42] employing the DNS data of a turbulent premixed round jet (Bunsen) flame. It was shown that the mean SGS variance $\langle V_\xi\rangle$ does not always represent an accurate estimation for the residual component and extra residual terms would arise unless the LES resolution is adequate to neglect them. Here, we follow the same ansatz for Q (as in work of Vervisch et al., but without introduction of the mass-weighted time averaging) which is expressed (by adding and subtracting the same terms) as:

$$Q \equiv \langle\xi^2\rangle - \langle\xi\rangle^2 = \underbrace{\langle\tilde{\xi}^2\rangle - \langle\tilde{\xi}\rangle^2}_{Q^W} + \underbrace{\left(\langle\widetilde{\xi^2}\rangle - \langle\tilde{\xi}^2\rangle\right)}_{\langle V_\xi\rangle} - \underbrace{\left(\langle\xi\rangle^2 - \langle\tilde{\xi}\rangle^2\right)}_{R_I} + \underbrace{\left(\langle\xi^2\rangle - \langle\widetilde{\xi^2}\rangle\right)}_{R_{II}}, \tag{21}$$

where $R_I(\Delta)$ and $R_{II}(\Delta)$ denote additional residual terms. Clearly, the modeling of these terms is undesirable in LES since it would imply the modeling of the fluctuating fields ξ'' and $(\xi^2)''$, or their time averages, in addition to the modeling of the mean SGS variance which depends solely on the resolved quantities. Thus, the LES turbulence resolution scale should be sufficiently small, say $\Delta < \Delta_V^*$, to guarantee that (1) both $R_I(\Delta)$ and $R_{II}(\Delta)$ are negligible, or (2) $R_I(\Delta) = R_{II}(\Delta)$, so the mean SGS variance can be used as a measure of the residual statistics. In [42], Vervisch and co-workers proposed such an LES resolution criterion which verifies the first case:

$$R_I = \left(\langle\xi - \tilde{\xi}\rangle\right)\left(\langle\xi + \tilde{\xi}\rangle\right) = \langle\xi''\rangle^2 + 2\langle\xi''\rangle\langle\tilde{\xi}\rangle = 0 \quad \Leftrightarrow \quad \langle\xi''\rangle = 0, \tag{22}$$

$$R_{II} = \langle\xi^2\rangle - \langle\widetilde{\xi^2}\rangle = 0 \quad \Leftrightarrow \quad \langle(\xi^2)''\rangle = 0. \tag{23}$$

The first equation here shows that $R_I = 0$ is satisfied automatically if one assumes that the mean mixture fraction is modeled according to Eq. 20 as the resolved mean field, which assumes $\Delta < \Delta_M^*$. The second equation, $R_{II} = 0$, on the other hand, necessitates that the time average of the residual fluctuations of the mixture fraction square is negligible which would most likely happen at even smaller scales, $\Delta < \Delta_V^* < \Delta_M^*$, since the square of the mixture fraction contains a wider range of scales than the mixture fraction field itself. Note that in the second case, i.e., when $R_I(\Delta) = R_{II}(\Delta)$ together with the assumption of Eq. 20, the mean SGS variance becomes the sole and exact representative of the residual statistic.

Finally, it should be appreciated that even if the LES resolution allows to neglect $R_{II}(\Delta)$ it does not guarantee that the sum of the resolved $Q^W(\Delta)$ and SGS $\langle V_\xi(\Delta)\rangle$ parts becomes independent of the turbulence resolution scale Δ which calls for a convergence study for $Q^m(\Delta)$ and modeling its limit at $\Delta = 0$. As a result, in the present work, the residual statistic $Q^r(\Delta)$ is modeled as the mean SGS variance $\langle V_\xi\rangle$ according to:

$$Q \approx Q^m(\Delta) = Q^W(\Delta) + Q^r(\Delta) = \left[\langle(\tilde{\xi})^2\rangle - \langle\tilde{\xi}\rangle^2\right] + \langle V_\xi\rangle, \tag{24}$$

where the first bracketed term represents the resolved mixture fraction variance.

In this paper, the LES statistics are accumulated after the simulation has reached a statistically-stationary state which was verified by the convergence in the rms statistics. This corresponds to the non-dimensional time of $tU_B/D = 690$ which is about 10 flow-through times based on the bulk velocity and the characteristic length of $70D$. After that, the simulation is continued for approximately twelve flow-through times (until $tU_B/D \approx 1500$) to accumulate statistics. The LES statistics are computed by averaging in time and the circumferential direction, for example $Q^m(x,r) = \langle\widetilde{U}\rangle(x,r)$. Thus, the convergence of the LES statistics is represented locally by $Q^m(\Delta(\boldsymbol{x})) = \mathcal{L}(\Delta(\boldsymbol{x}))$, where $\mathcal{L}(\Delta)$ are different functions at each point of the computational domain Ω. On the other hand, employing a global relation based an integral norm, $\|Q^m\|_2 = \mathcal{G}(\|\Delta\|_2)$, i.e., where the norm is defined as $\|Q^m\|_2 = 1/|\Omega|\left(\int_\Omega Q^{m2} d\boldsymbol{x}\right)^{1/2}$, is expected to produce more robust statistical estimates with less variation in $\|\Delta\|_2$. However, this approach would not allow to identify local flow regions which would require more (or less) resolution, and therefore, it has not been pursued in the current work.

4 Results

In this section we analyze the effect of three SGS models (the dynamic Smagorinsky model (DSMG), the standard Vreman model (Vreman-I) and the Vreman model where the model constant doubled (Vreman-II) on the LES statistics of the velocity

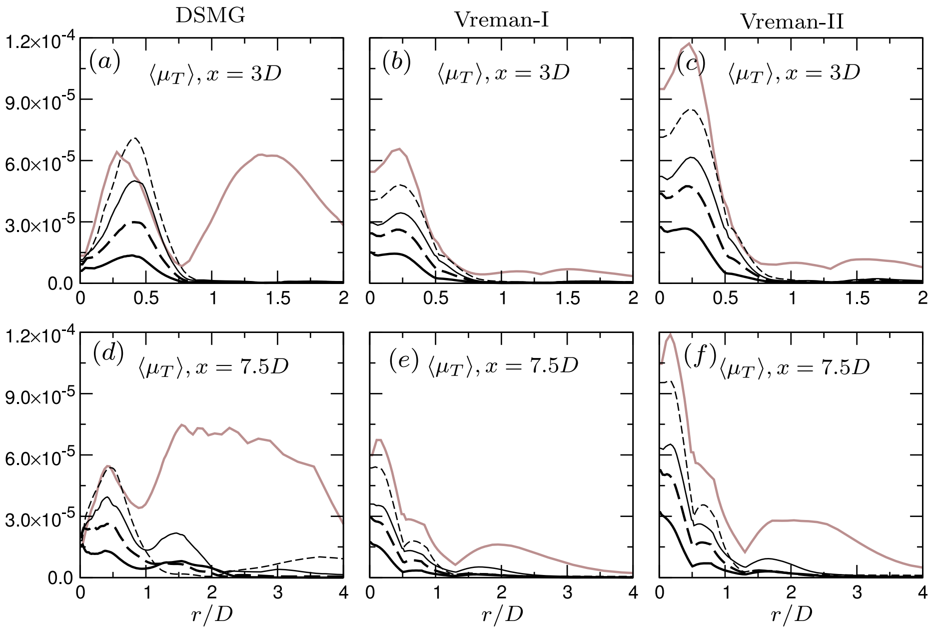

Fig. 3 Radial profiles of the normalized subgrid eddy viscosity $\langle\mu_T\rangle$ at $x = 3D$ and $7.5D$: DSMG (**a**, **d**), Vreman-I (**b**, **e**), Vreman-II (**c**, **f**), and for grids M_1—*gray line*, M_2—*thin dashed line*, M_3—*thin solid line*, M_4—*dashed line*, M_5—*solid line*

and mixture fraction fields. Here, we primarily focus on the spatial convergence of first two moments, i.e., the statistical mean and variance, with respect to the resolution scale $\Delta(\boldsymbol{x})$. But first, we start with a brief discussion of the results obtained on the subgrid viscosity.

4.1 Subgrid viscosity

It is well known that while the subgrid eddy-viscosity models provide a simple way to account for the mainly dissipative action of the unresolved sales they sometimes, and DSMG model in particular, require an introduction of additional, and very often ad-hoc, procedures involving explicit filtering, averaging and clipping to prevent negative values of the subgrid eddy viscosity which could lead to unstable LES calculations. In the present work, the test filtering operation required for evaluation of the dynamic constant C_μ in DSMG model is performed only in the axial and circumferential directions. Furthermore, the instantaneous values of C_μ are obtained by employing averaging in the homogeneous (circumferential) direction, and as a result, they depend on the axial and radial directions only, $C_\mu(x, r)$. In addition, the negative values of C_μ is then clipped to zero enforcing $\mu_T \geq 0$. The Vreman SGS model, on the other hand, guarantees non-negative values of μ_T by formulation and does not involve explicit filtering and averaging.

The radial profiles of the time averaged subgrid eddy viscosity (normalized by the jet reference values) are shown in Figs. 3, 4, and 5 for all three models. In

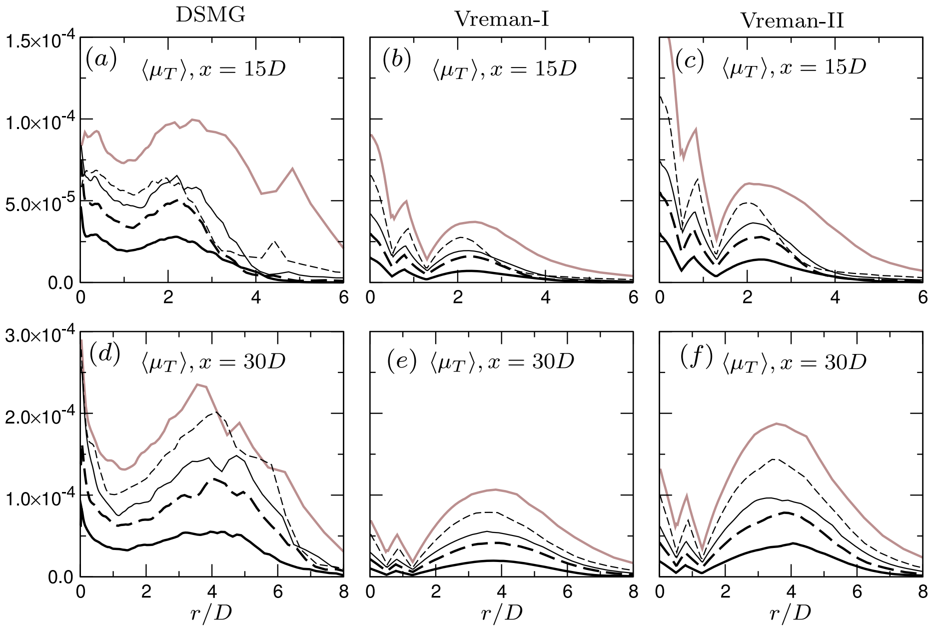

Fig. 4 Radial profiles of the normalized subgrid eddy viscosity $\langle\mu_T\rangle$ at $x = 15D$ and $30D$: DSMG (**a**, **d**), Vreman-I (**b**, **e**), Vreman-II (**c**, **f**)

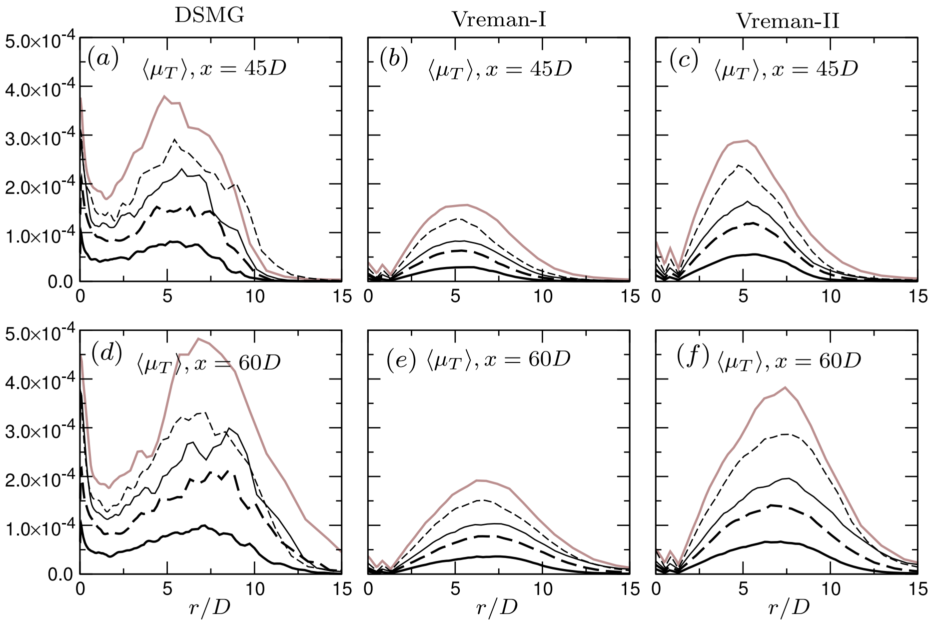

Fig. 5 Radial profiles of the normalized subgrid eddy viscosity $\langle\mu_T\rangle$ at $x = 45D$ and $60D$: DSMG (**a**, **d**), Vreman-I (**b**, **e**), Vreman-II (**c**, **f**)

the jet near-field ($x/D \leq 7.5$) the subgrid eddy-viscosity of DSMG model is seen to be comparable in magnitude with that of Vreman-I model with an exception of the coarsest grid M_1, where it is too dissipative in the transitional region between pilot products and co-flow air. As the jet develops and spreads outward, the subgrid viscosity grows and overcomes the corresponding values obtained with both Vreman models for all five grids. Figures 4d and 5a, d also show that the DSMG model produces somewhat excessive values of the subgrid eddy viscosity close to the centerline at farther downstream locations ($x/D \geq 30$). This can be related to the test filtering procedure employed in the current computation of C_μ which excludes filtering in the radial direction. Here, the resolved velocity gradients show small changes in magnitude when they are computed at the test filter level. The denominator in the definition of C_μ depends on the difference between test-filtered resolved strain rate $\widehat{|\widetilde{S}|\widetilde{S}_{ij}}$ and the test-filtered strain rate $|\widehat{\widetilde{S}}|\widehat{\widetilde{S}}_{ij}$ (multiplied by the square of the ratio of the test to grid level filters). This difference becomes small near the centerline which results in high values of C_μ and, correspondingly, the subgrid eddy viscosity.

A comparison of two Vreman models shows that Vreman-II model is characterized by approximately 60–90% higher values of the subgrid viscosity than those of Vreman-I model for most of the flow domain, except the near field ($x/D < 7.5$) where the ratio of the corresponding viscosities becomes approximately equal to two. This is expected because of the doubled value of C_v used in Vreman-II case. Note that non-monotonic behavior of the subgrid viscosity for $r/D \leq 1.5$ is the consequence of the radial grid stretching close to the pilot and nozzle walls.

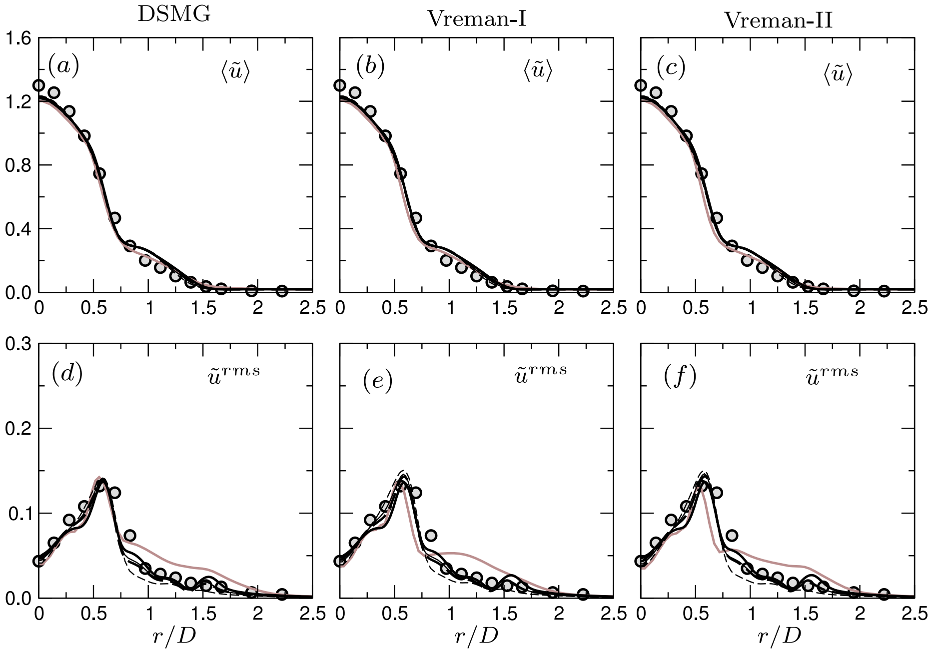

Fig. 6 Radial profiles of $\langle\tilde{u}\rangle$ and $\tilde{u}^{\mathrm{rms}}$ at $x = 3D$: DSMG (**a**, **d**), Vreman-I (**b**, **e**), Vreman-II (**c**, **f**). M_1—*gray line*, M_2—*thin dashed line*, M_3—*thin solid line*, M_4—*dashed line*, M_5—*solid line*, experiment—*circles* [24]

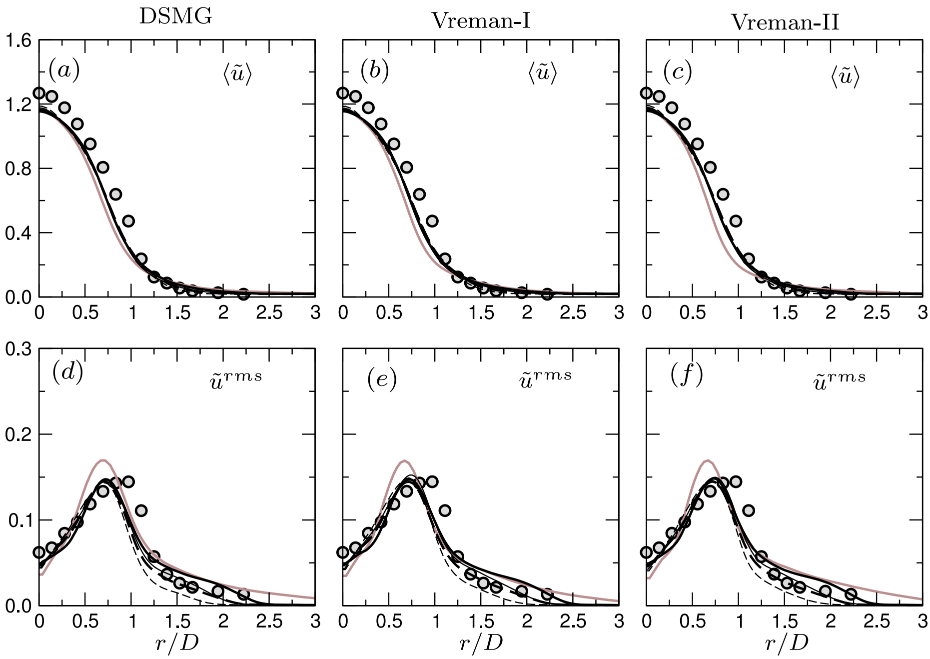

Fig. 7 Radial profiles of $\langle\tilde{u}\rangle$ and $\tilde{u}^{\mathrm{rms}}$ at $x = 7.5D$: DSMG (**a**, **d**), Vreman-I (**b**, **e**), Vreman-II (**c**, **f**)

4.2 Resolved velocity field

Figures 6, 7, 8, 9, 10, and 11 show profiles of the mean and rms of the streamwise velocity (normalized by the bulk jet velocity) at six axial locations of $x/D = 3$, 7.5, 15, 30, 45 and 60 for DSMG, Vreman-I and Vreman-II models. It is seen that all three SGS models demonstrate a good level of approximation of the experimental data with the highest discrepancy observed in the rms fields and on the coarsest M_1 grid. The mean LES velocity is characterized by the consistent convergence at all axial locations and exhibits little sensitivity to a choice of the employed SGS model.

The rms of LES velocity is also found to be convergent for the most part of the flow with a noticeable exception of axial locations of $x/D = 30$ and 45 (Figs. 9 and 10) where the sensitivity to the grid resolution can be observed in a small region of $0 < r/D < 2.0$, i.e., around the peak value of the rms profile. Here, the rms of the resolved velocity is the highest on the coarsest grid and experiences the convergence "from above", thus attaining the lower values on the finer grids. This sensitivity to the grid resolution gradually decays downstream and becomes weak at $x/D = 60$. This is most likely caused by the better resolution of velocity gradients on finer grids which, in turn, increases the viscous dissipation rate, thus resulting in lower values of the rms velocity fluctuations. Beyond a radial location of $r/D \approx 1.7$ the rms of resolved velocity is seen to be convergent as shown in Fig. 9d, e, f. It is interesting to note that this location approximately corresponds to the location of the stoichiometric mixture fraction $\tilde{\xi}_{st}$, which means that the highest Δ-dependence is observed on the fuel-rich side of the jet. Figures 6 and 7 show another region where the velocity rms is

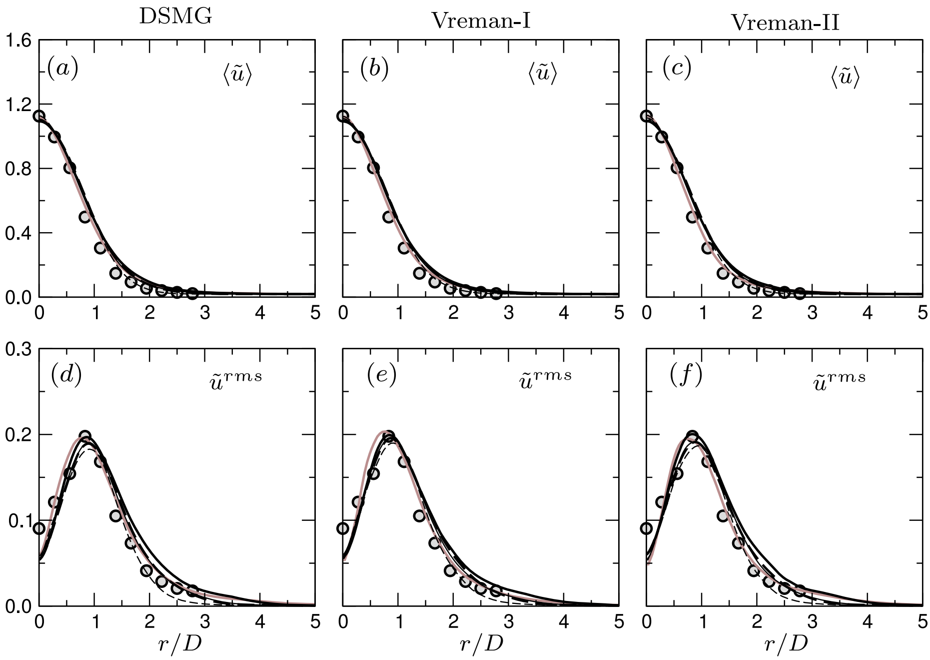

Fig. 8 Radial profiles of $\langle\tilde{u}\rangle$ and $\tilde{u}^{\mathrm{rms}}$ at $x = 15D$: DSMG (**a**, **d**), Vreman-I (**b**, **e**), Vreman-II (**c**, **f**)

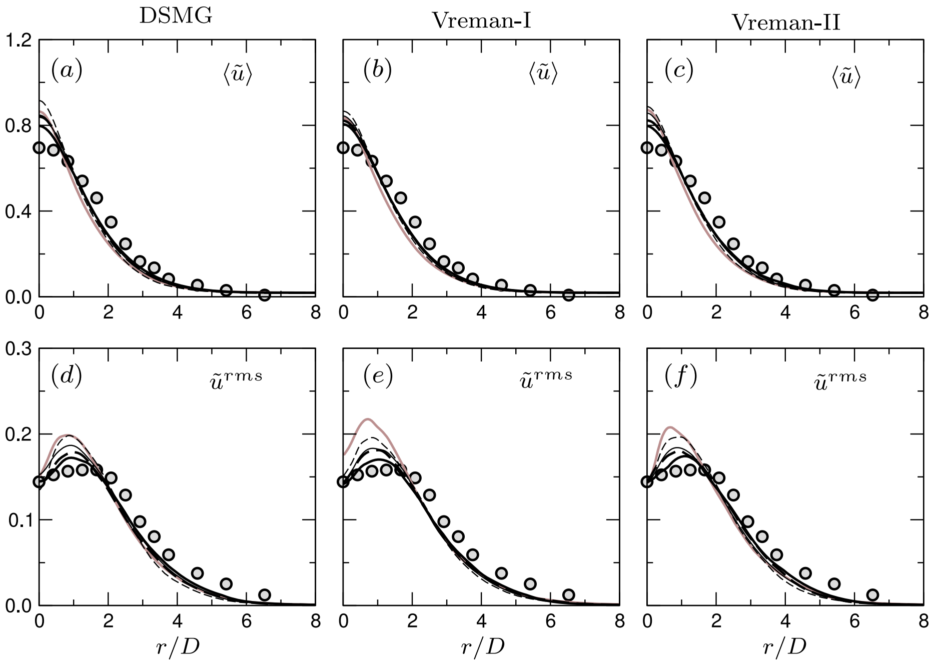

Fig. 9 Radial profiles of $\langle\tilde{u}\rangle$ and $\tilde{u}^{\mathrm{rms}}$ at $x = 30D$: DSMG (**a**, **d**), Vreman-I (**b**, **e**), Vreman-II (**c**, **f**)

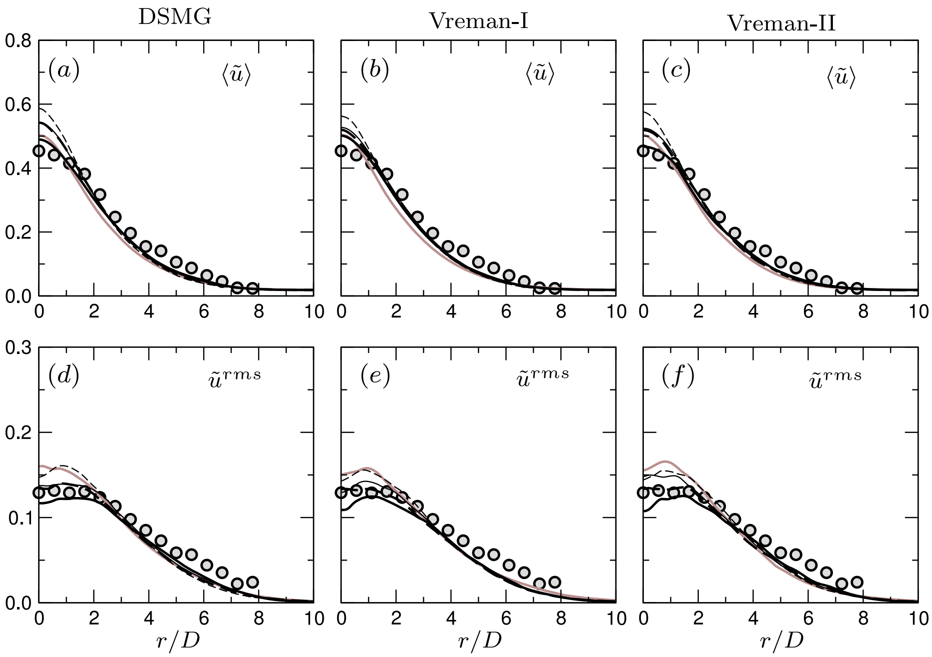

Fig. 10 Radial profiles of $\langle\tilde{u}\rangle$ and $\tilde{u}^{\mathrm{rms}}$ at $x = 45D$: DSMG (**a**, **d**), Vreman-I (**b**, **e**), Vreman-II (**c**, **f**)

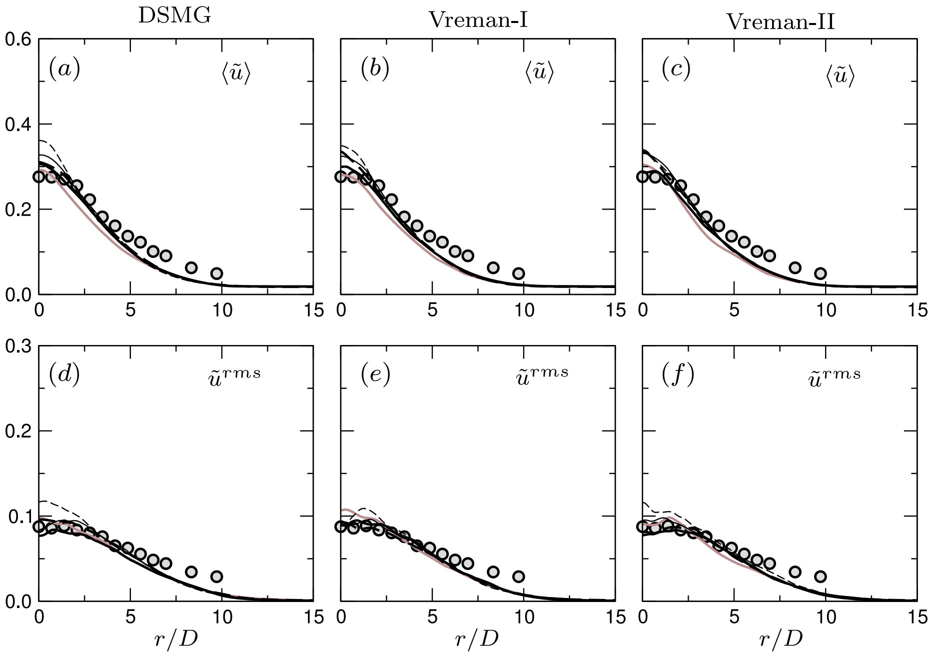

Fig. 11 Radial profiles of $\langle\tilde{u}\rangle$ and $\tilde{u}^{\mathrm{rms}}$ at $x = 60D$: DSMG (**a**, **d**), Vreman-I (**b**, **e**), Vreman-II (**c**, **f**)

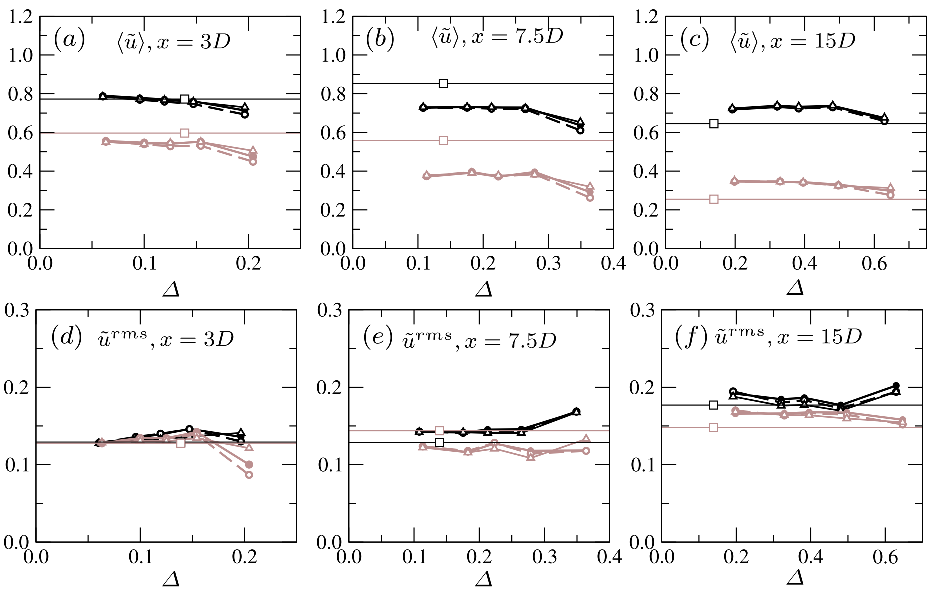

Fig. 12 Convergence of $\langle\tilde{u}\rangle$ and $\tilde{u}^{\mathrm{rms}}$ at the axial and two radial locations—closer to (*dark lines*) and farther from (*light lines*) the centerline: (**a**, **d**) $x = 3D$, $r_1 = 0.54D$, $r_2 = 0.63D$; (**b**, **e**) $x = 7.5D$, $r_1 = 0.65D$, $r_2 = 0.9D$; (**c**, **f**) $x = 15D$, $r_1 = 0.7D$, $r_2 = 1.2D$, and for: DSMG (△), Vreman-I (●), Vreman-II (○) and experiment (□). Each point (from *right* to *left*) corresponds to grids $M_1 - M_5$. The experimental values correspond to the resolution $\Delta^U_{\mathrm{exp}} = 0.139D$

visibly dependent on Δ. This region corresponds to a mixing layer between hot pilot products and cold co-flow air ($0.8 < r/D < 1.6$ at $x/D = 3$). Here, the turbulence is very weak and the mixing layer is dominated by coherent vortical structures which can be sensitive to the grid resolution due to the specification of the pilot inflow velocity fluctuations and incurred numerical errors.

The dependence of the resolved velocity statistics on Δ at particular axial and radial locations are shown in Figs. 12 and 13. For each axial locations the two radial locations are considered, one on the left side of the location of the rms velocity maximum and the other on the right side, closer to the lean side of the jet. In addition, the experimental values as measured by Schneider et al. [24] are shown by horizontal lines with the experimental resolution scale corresponding to a square symbol. For all three SGS models the mean of the resolved velocity demonstrates negligible dependence on the turbulence resolution scale starting with Δ_2 (M_2 grid) with the highest dependence observed at the near-field location of $x/D = 3, r/D = 0.54$. This is shown in Fig. 12a where the mean velocity weakly increases with a decrease in Δ in approximately linear fashion. Note that at this location the experimental resolution scale is only little better than that of grid M_2. Overall, at all considered locations the mean of the resolved velocity exhibits the linear dependence on Δ for the four finest grids. Similarly, with the exception of the coarsest grid M_1, the rms velocity statistics are also characterized by approximately linear behavior with respect to Δ for most locations as can be seen from Figs. 12 and 13d, e, f. The Δ-dependence of the rms velocity statistics is more pronounced but still relatively weak. Nevertheless, Fig. 13d

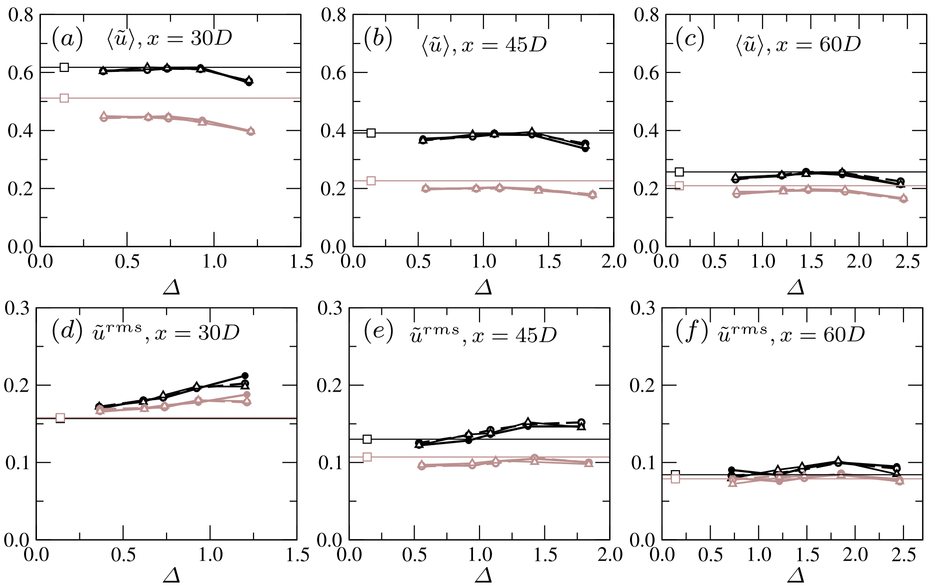

Fig. 13 Convergence of $\langle\tilde{u}\rangle$ and $\tilde{u}^{\mathrm{rms}}$ at the axial and two radial locations—closer to (*dark lines*) and farther from (*light lines*) the centerline: (**a**, **d**) $x = 30D, r_1 = 0.9D, r_2 = 1.4D$; (**b**, **e**) $x = 45D, r_1 = 1.5D, r_2 = 3D$; (**c**, **f**) $x = 60D, r_1 = 2D, r_2 = 3D$, and for: DSMG (△), Vreman-I (●), Vreman-II (○) and experiment (□). Each point (from *right* to *left*) corresponds to grids $M_1 - M_5$. The experimental values correspond to the resolution $\Delta^U_{\mathrm{exp}} = 0.139D$

shows that at $x/D = 30$, $r/D = 0.9$ the extrapolated value of the rms velocity at $\Delta = 0$ ($\tilde{u}_{\circ}^{\mathrm{rms}} \approx 0.155$) is approximately 12% less than that on M_5 grid ($\tilde{u}_{M_5}^{\mathrm{rms}} \approx 0.175$) and is approximately 20% less than that on M_2 grid ($\tilde{u}_{M_2}^{\mathrm{rms}} \approx 0.195$). Thus, a procedure for estimating the DNS limiting values of the statistics is important for assessment of the solution quality.

Figures 12 and 13 show that the Vreman SGS model produces resolved velocity statistics which are very close to that of DSMG model, thus confirming the findings of the original Vreman's paper obtained for simpler turbulent flows [22]. From these figures it is seen that the effect of the Vreman model constant C_v on the resolved velocity statistics is almost negligible, especially for the mean velocity and on the four finer grids. Generally, the higher value of Vreman constant (as in Vreman-II model) tends to decrease the rms velocity fluctuations due to the higher level of the

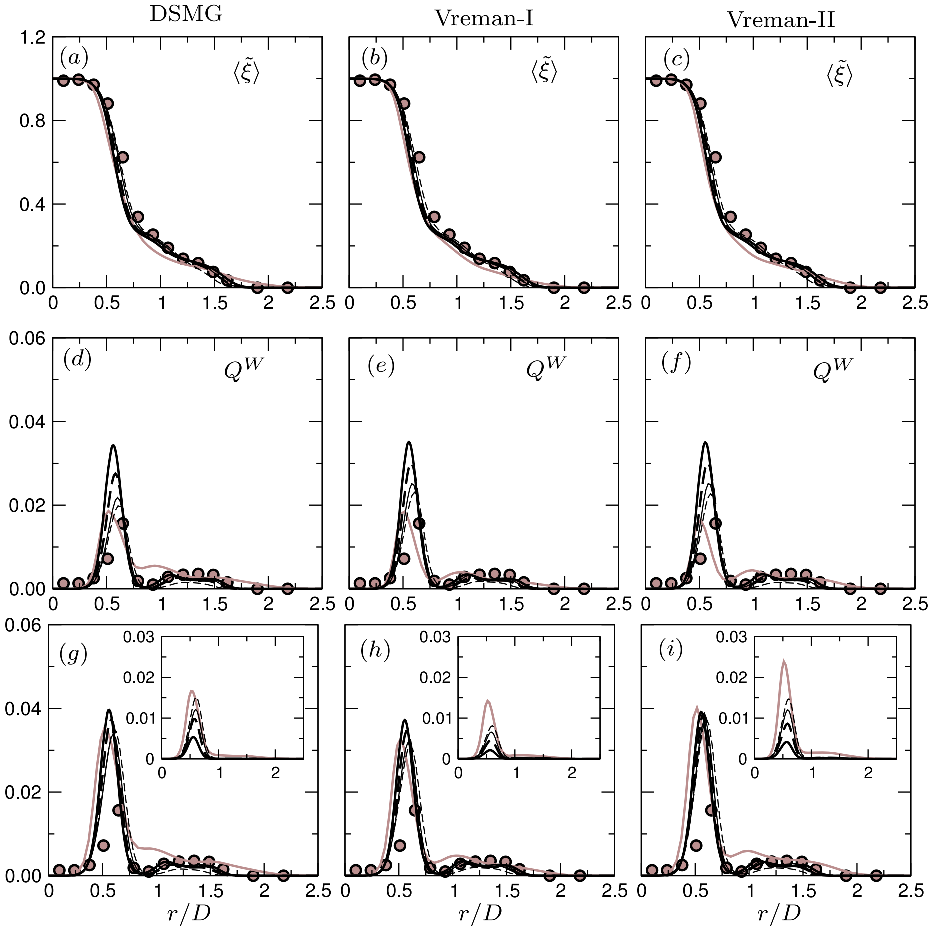

Fig. 14 Radial profiles of $\langle\tilde{\xi}\rangle$ (*top row*), $Q^W = (\tilde{\xi}^{\mathrm{rms}})^2$ (*middle row*) and total variance Q^m (*bottom row*) at $x = 3D$: DSMG (**a**, **d**, **g**), Vreman-I (**b**, **e**, **h**), Vreman-II (**c**, **f**, **i**). *Insets* show residual variance, $Q^r = \langle V_\xi \rangle$. M_1—*gray line*, M_2—*dashed thin line*, M_3—*solid thin line*, M_4—*dashed line*, M_5—*solid line*, experiment—*circles* [23]

subgrid eddy viscosity, but this effect is very small for $M_2 - M_5$ grids as can be seen from Fig. 12d, e, f. Thus, the relative insensitivity of the velocity statistics to the value of Vreman constant suggests that requirements for its dynamic evaluation procedure [40] can be somewhat eased once an LES grid is sufficiently fine.

4.3 Resolved mixture fraction field

Radial profiles of the mean mixture fraction as well as the resolved variance $Q^W = \langle \tilde{\xi}^2 \rangle - \langle \tilde{\xi} \rangle^2$, mean SGS variance $Q^r = \langle V_\xi \rangle$ and total variance $Q^m = Q^W + Q^r$ of the mixture fraction are shown in Figs. 14, 15, 16, 17, 18, and 19 at six axial locations of $x/D = 3$, 7.5, 15, 30, 45 and 60. In these figures the experimental data of Barlow and Frank [23] are also depicted for comparison.

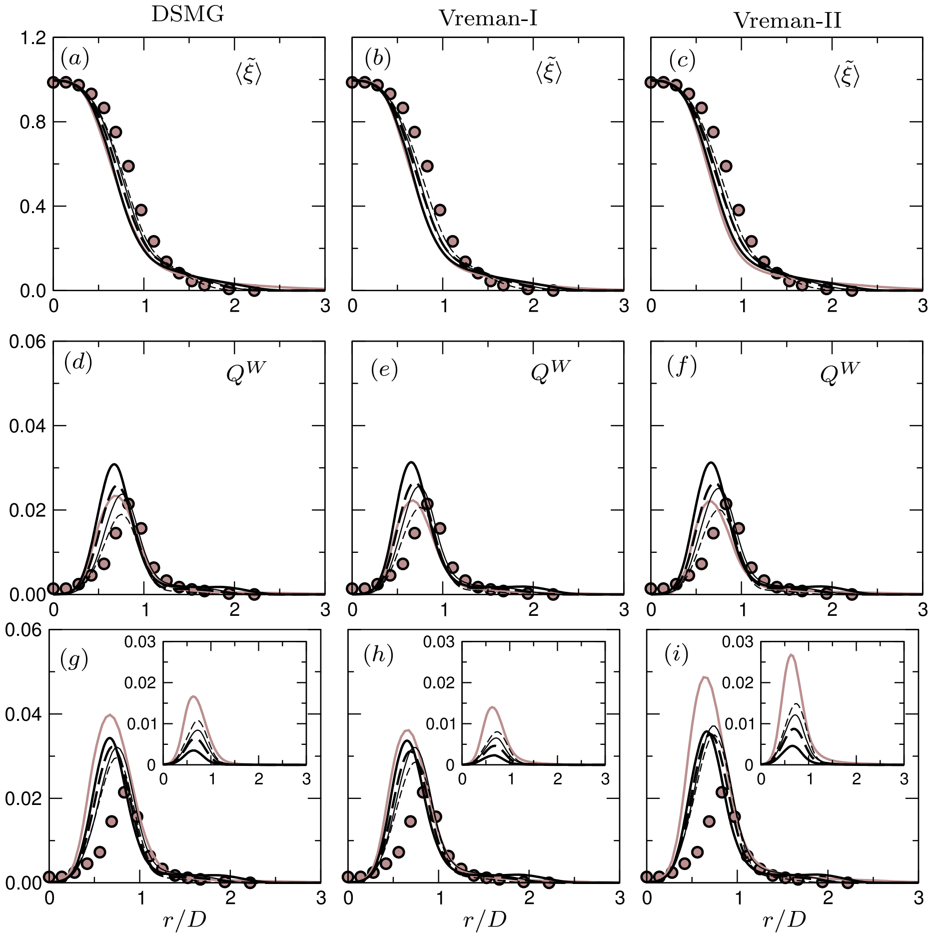

Fig. 15 Radial profiles of $\langle \tilde{\xi} \rangle$ (*top row*), $Q^W = (\tilde{\xi}^{\mathrm{rms}})^2$ (*middle row*) and total variance Q^m (*bottom row*) at $x = 7.5D$: DSMG (**a**, **d**, **g**), Vreman-I (**b**, **e**, **h**), Vreman-II (**c**, **f**, **i**). *Insets* show residual variance, $Q^r = \langle V_\xi \rangle$

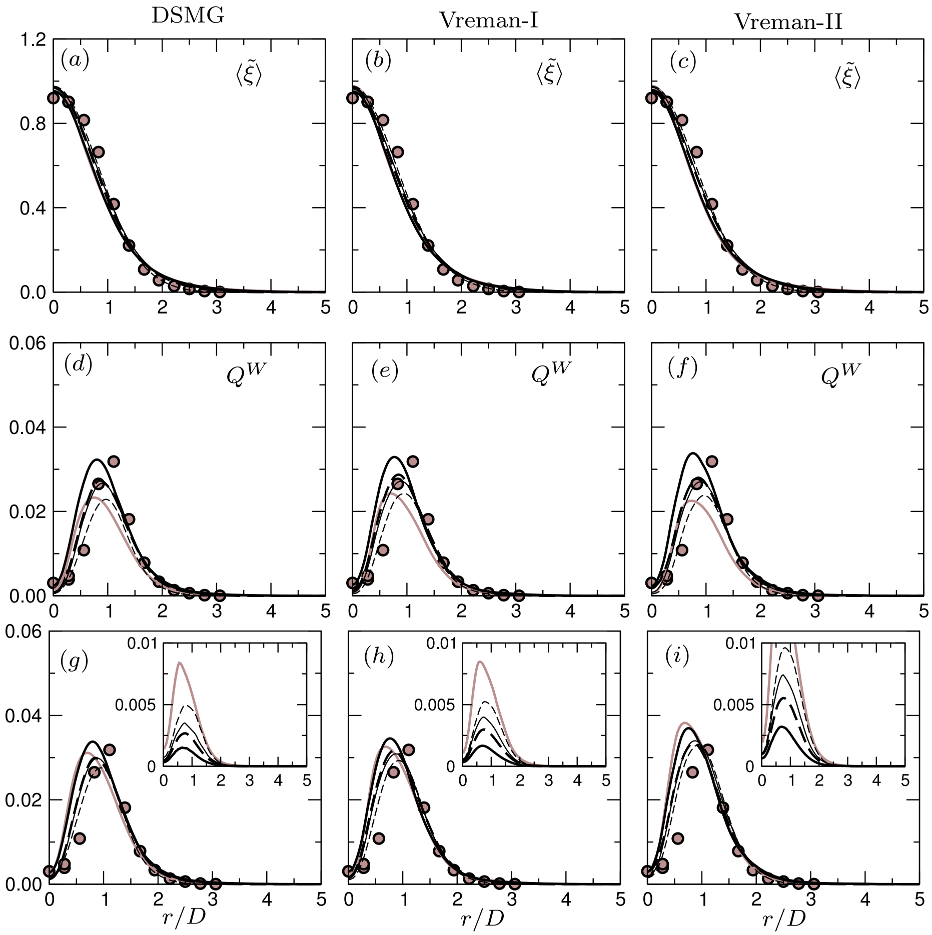

Fig. 16 Radial profiles of $\langle\tilde{\xi}\rangle$ (*top row*), $Q^W = (\tilde{\xi}^{\mathrm{rms}})^2$ (*middle row*) and total variance Q^m (*bottom row*) at $x = 15D$: DSMG (**a**, **d**, **g**), Vreman-I (**b**, **e**, **h**), Vreman-II (**c**, **f**, **i**). *Insets* show residual variance, $Q^r = \langle V_\xi \rangle$

The mean mixture fraction fields demonstrate approximate convergence on $M_2 - M_5$ grids in most of the domain for all three SGS models being in good agreement with the experimental data. There is, however, a small region near the centerline at the downstream location of $x/D \geq 30$ where some dependency on Δ is visible, as can be seen from Figs. 17–19a–c. This can be related to the corresponding dependence observed in the resolved velocity field (Figs. 9–11a–c) which suggests the inadequate grid resolution in the streamwise direction at this axial location as might be inferred from the axial dependence of $\Delta(x, 0)$ shown in Fig. 2a.

In general, it is expected that the variance fields are more susceptible to the influence of the turbulence resolution scale Δ [20], which finds confirmation in Figs. 14–19d–i. From these figures it is seen that in the near-field the resolved variances exhibit a visible sensitivity to Δ at the locations of their maxima, i.e., in a mixing layer between cold jet fuel and hot pilot products. Here, the resolved

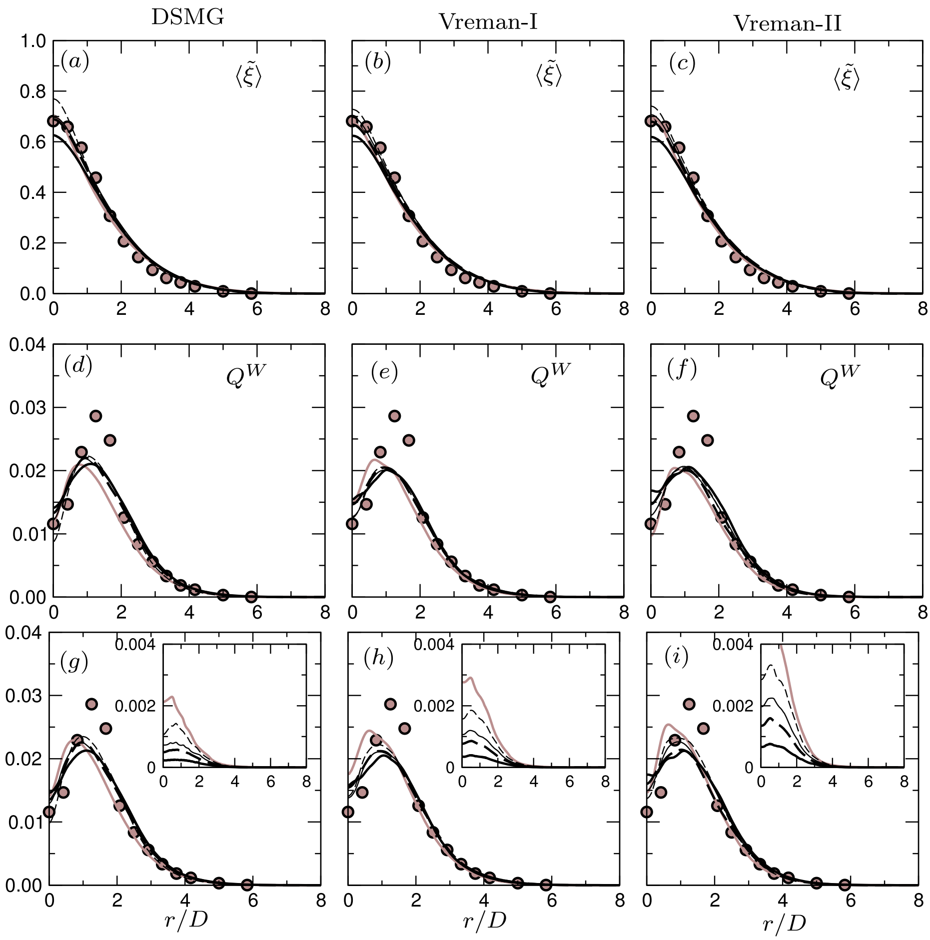

Fig. 17 Radial profiles of $\langle\tilde{\xi}\rangle$ (*top row*), $Q^W = (\tilde{\xi}^{\mathrm{rms}})^2$ (*middle row*) and total variance Q^m (*bottom row*) at $x = 30D$: DSMG (**a**, **d**, **g**), Vreman-I (**b**, **e**, **h**), Vreman-II (**c**, **f**, **i**). *Insets* show residual variance, $Q^r = \langle V_\xi \rangle$

variance is found to be overpredicting the experimental values on the finer grids. As the jet develops, the resolved variance becomes in general agreement with the experimental values at $x/D = 15$, and eventually it underpredicts the experimental values downstream starting with $x/D = 30$. In the near-field region the resolved variance is characterized by the convergence from below where the higher variance values are attained on the finer grids. This can be related to a strong decrease of the turbulent subgrid diffusivity $\bar{\rho}D_T$ as grids are more and more refined, while the molecular diffusivity $\bar{\rho}\widetilde{D}$ remains relatively unchanged and smaller than its peak values because of temperature [32]. Therefore, changes in turbulent subgrid diffusivity is contributing more to changes of the total diffusivity which results in less dissipation for finer grids and causes higher values of the resolved mixture fraction variance. Farther downstream, for example at $x/D = 30$, the resolved mixture fraction variance shows less sensitivity to Δ and is closer to an approximate convergent

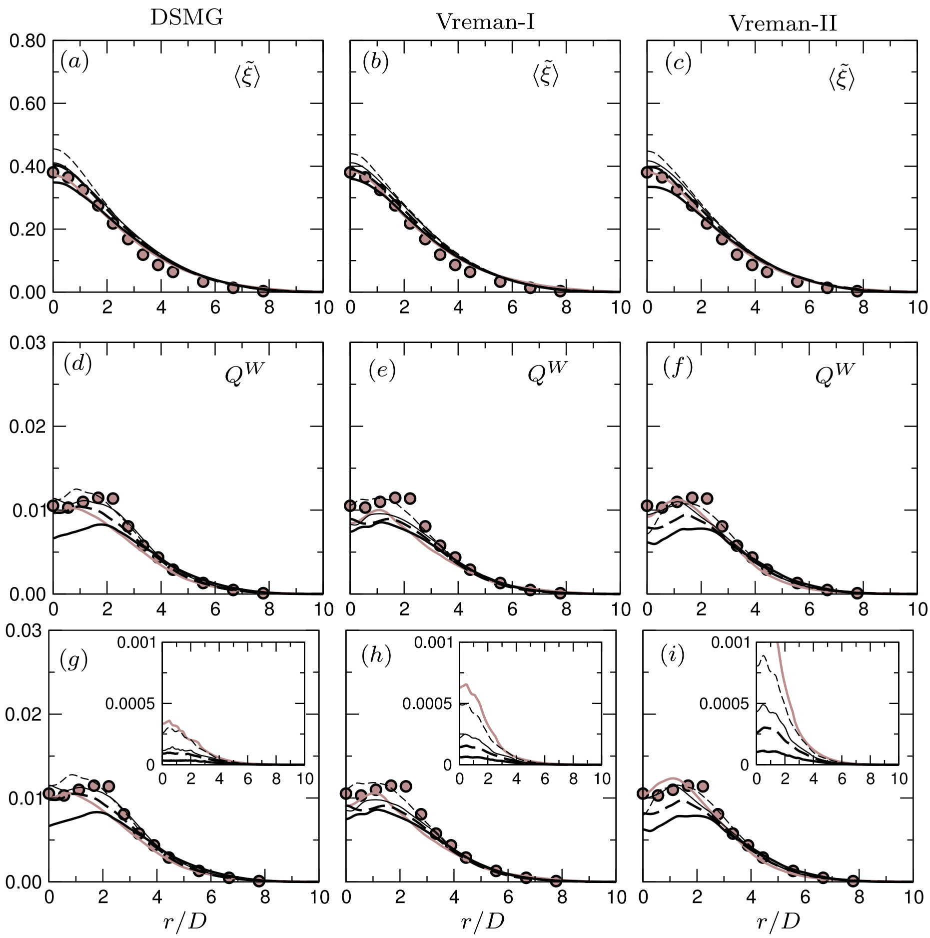

Fig. 18 Radial profiles of $\langle\tilde{\xi}\rangle$ (*top row*), $Q^W = (\tilde{\xi}^{\mathrm{rms}})^2$ (*middle row*) and total variance Q^m (*bottom row*) at $x = 45D$: DSMG (**a**, **d**, **g**), Vreman-I (**b**, **e**, **h**), Vreman-II (**c**, **f**, **i**). *Insets* show residual variance, $Q^r = \langle V_\xi \rangle$

state on all $M_1 - M_5$ grids (Fig. 17). Here, some weak dependence on Δ is still present which resembles the behavior of the rms velocity and shows convergence from above. Figures 18 and 19d–f show that for the farthest downstream locations of $x/D = 45$ and 60, the resolved variance again exhibits a significant sensitivity to Δ in a region of $0 < r/D < 3.0$, similar to the mean mixture fraction field. In addition to the above mentioned reason of the insufficient resolution (due to the axial grid stretching), it is remarked that these far field locations also require longer computational runs to accumulate an equivalent statistical data compared to near-field locations.

Figures 14–19g–i show the radial profiles of the SGS $Q^r(\Delta) = \langle V_\xi \rangle$ and total $Q^m(\Delta)$ variances of the mixture fraction field. It is seen that in the near-field, the SGS variance contribution can be quite substantial. For example, at an axial location of $x/D = 3$ it ranges approximately from 70% (on M_1 grid) to 10% (on M_5 grid) of the

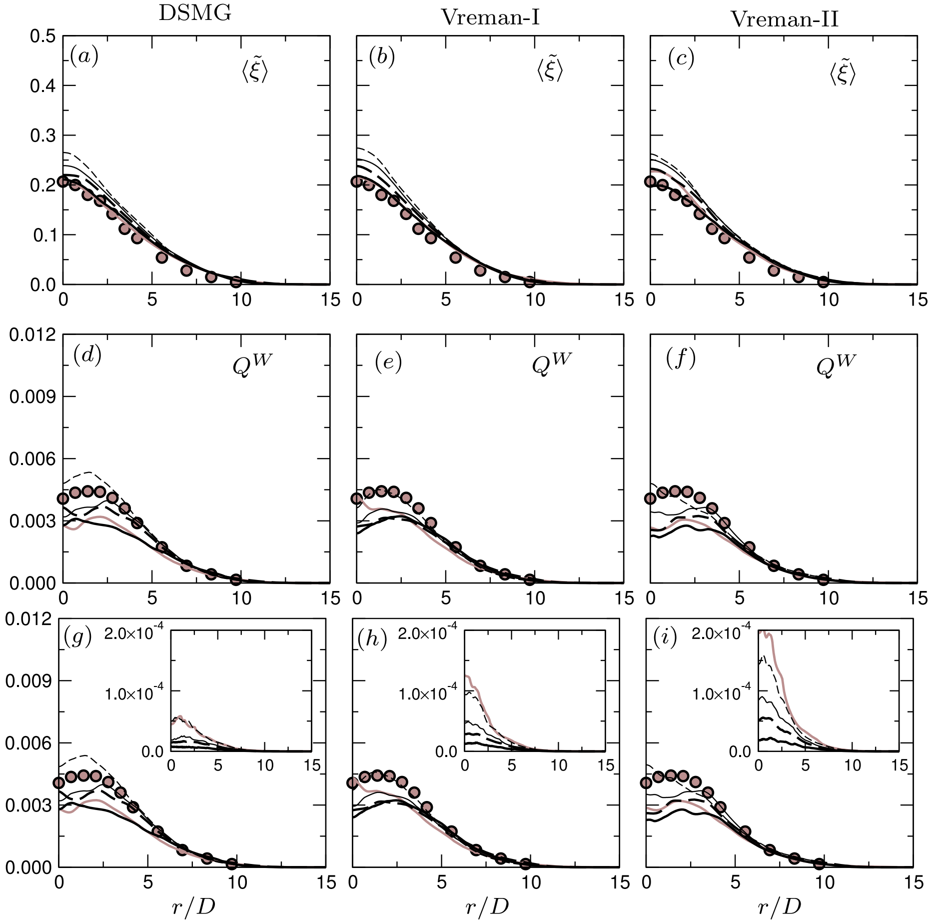

Fig. 19 Radial profiles of $\langle\tilde{\xi}\rangle$ (*top row*), $Q^W = (\tilde{\xi}^{\mathrm{rms}})^2$ (*middle row*) and total variance Q^m (*bottom row*) at $x = 60D$: DSMG (**a**, **d**, **g**), (ii) Vreman-I (**b**, **e**, **h**), (iii) Vreman-II (**c**, **f**, **i**). *Insets* show residual variance, $Q^r = \langle V_\xi \rangle$

corresponding peak values of the resolved variance. Note, however, that would be equivalent to only 30% and 5% contribution to the corresponding values of the rms of the resolved mixture fraction, respectively. On the other hand, the SGS variance rapidly decreases downstream and becomes an order of magnitude smaller than the resolved variance already at $x/D = 30$ for the coarsest M_1 grid. Its contribution to the total variance appears to be not sufficient to compensate the underprediction of the experimental values by the resolved variance Q^W. This suggests a non-constant value of the model coefficient C in the SGS dissipation rate model given by Eq. 5, which can be achieved, for example, by employing a dynamic procedure [43]. It is further noted that while a model for Q^m could be, in principle, improved for some resolution levels ($\Delta > \Delta_V^*$) by accounting for extra residual terms (as outlined in Section 3.3), an ultimate goal of LES is to estimate the limiting value of $Q^m(\Delta)$ at $\Delta = 0$. Therefore, the simpler residual models for Q^r could be more advantageous and robust as long as they ensure that $Q^r(\Delta)$ vanishes at $\Delta = 0$.

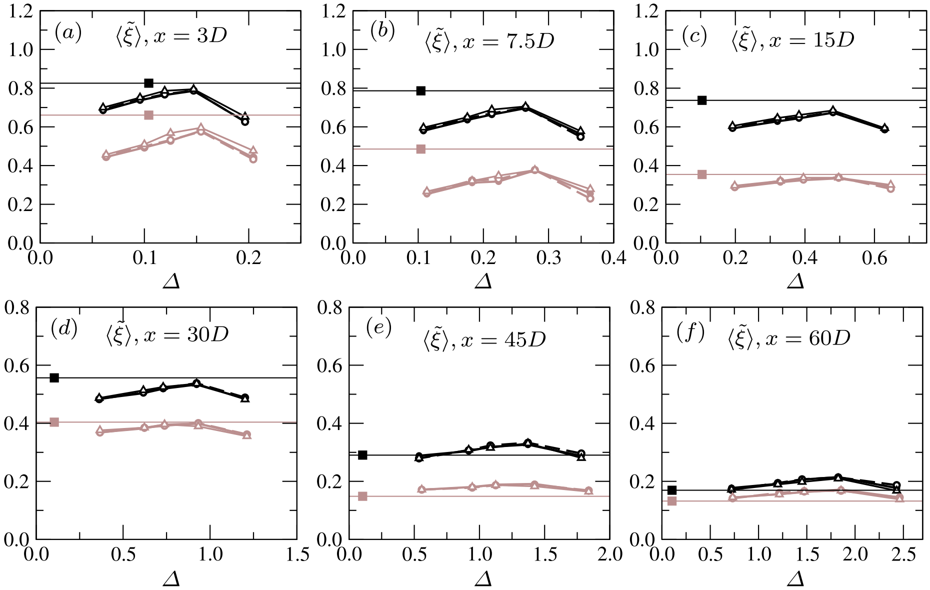

Fig. 20 Convergence of $\langle\tilde{\xi}\rangle$ at the axial and two radial locations—closer to (*dark lines*) and farther from (*light lines*) the centerline: **a** $x = 3D$, $r_1 = 0.54D$, $r_2 = 0.63D$; **b** $x = 7.5D$, $r_1 = 0.65D$, $r_2 = 0.9D$; **c** $x = 15D$, $r_1 = 0.7D$, $r_2 = 1.2D$; **d** $x = 30D$, $r_1 = 0.9D$, $r_2 = 1.4D$; **e** $x = 45D$, $r_1 = 1.5D$, $r_2 = 3D$; **f** $x = 60D$, $r_1 = 2D$, $r_2 = 3D$, and for: DSMG (△), Vreman-I (●), Vreman-II (○) and experiment (■). Each point (from *right* to *left*) corresponds to grids $M_1 - M_5$. The experimental values correspond to the resolution $\Delta^S_{\mathrm{exp}} = 0.104D$

The dependence of the resolved mixture fraction statistics on the turbulence resolution scale is further shown in Figs. 20, 21, and 22. Here, the mean values of the mixture fraction as well as the resolved, SGS and total variances of the mixture fraction are plotted versus Δ for particular axial and radial locations. For comparison purposes, the corresponding experimental mean and variance values are also visualized at the experimental resolution scale Δ^S_{exp} [23]. Figure 20a–b shows that in the near-field (for $x/D = 3$ and 7.5) the mean mixture fraction experiences clear dependence on Δ. The largest differences between the extrapolated value of the mean mixture fraction $\langle\tilde{\xi}_\circ\rangle$ (at $\Delta = 0$) and its values on M_2 and M_5 grids, respectively, are observed at the location of $x/D = 7.5$, $r/D = 0.65$. Here, as can be seen from Fig. 20b, the extrapolated value ($\langle\tilde{\xi}_\circ\rangle \approx 0.5$) is about 28% less than that on M_2 grid ($\langle\tilde{\xi}_{M_2}\rangle \approx 0.7$) and 14% less than that on M_5 grid ($\langle\tilde{\xi}_{M_5}\rangle \approx 0.58$). As the jet develops downstream this Δ-dependence becomes weaker and the mean mixture fraction profiles become more flat, suggesting proximity to the converged state. For example, at axial locations of $x/D = 15$ and 30 the corresponding differences in the mean mixture fractions decrease to 21% and 10% (for M_2 and M_5 grids) and to 17% and 9%, respectively (Fig. 20c, d). Farther downstream at $x/D = 60$ and $r/D = 2$, in spite of the larger resolution scales the mean mixture fraction retains approximately the similar Δ-convergence rate as can be seen from Fig. 20f, where the extrapolated value $\langle\tilde{\xi}_\circ\rangle$ is about 30% and 11% less than the corresponding values computed on M_2 and M_5 grids, respectively. Overall, Fig. 20 shows that similarly to the mean

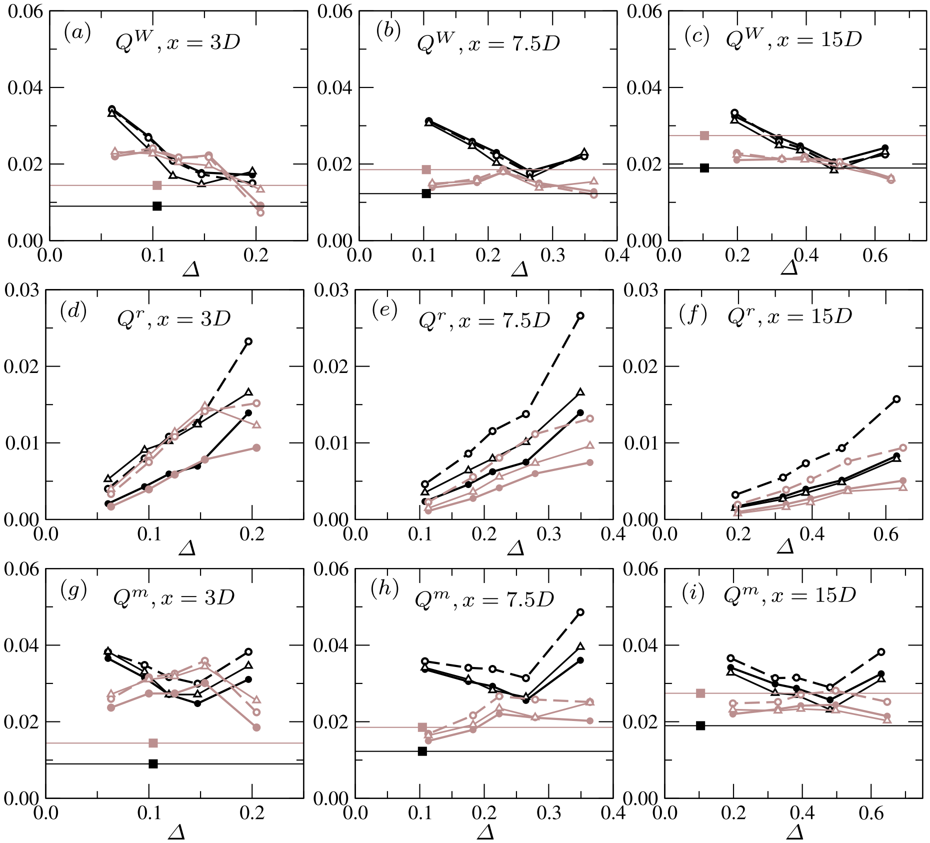

Fig. 21 Convergence of the mixture fraction variances: $Q^W(\Delta)$, $Q^r(\Delta)$ and $Q^m(\Delta)$ at the axial and two radial locations—closer to (*dark lines*) and farther from (*light lines*) the centerline: (**a**, **d**, **g**) $x = 3D$, $r_1 = 0.54D$, $r_2 = 0.63D$; (**b**, **e**, **h**) $x = 7.5D$, $r_1 = 0.65D$, $r_2 = 0.9D$; (**c**, **f**, **i**) $x = 15D$, $r_1 = 0.7D$, $r_2 = 1.2D$, and for: DSMG (△), Vreman-I (●), Vreman-II (○) and experiment (■). Each point (from *right* to *left*) corresponds to grids $M_1 - M_5$. The experimental values correspond to the resolution $\Delta^S_{\text{exp}} = 0.104D$

resolved velocity, the mean mixture fraction is characterized by (1) an approximate linear dependence on Δ starting from M_2 grid, (2) very little dependence on the SGS models, and (3) negligible sensitivity to a value of Vreman constant (for Vreman SGS models).

Figures 21a–c and 22a–c show profiles of the resolved mixture fraction variance $Q^W(\Delta)$. The fuel-rich side locations are characterized by a strong dependence on Δ which becomes approximately linear downstream at axial locations of $x/D = 7.5$ and 15 for $M_2 - M_5$ grids. At these locations the extrapolated values of the resolved mixture fraction variance ($Q^W_\circ$) are almost two times higher than those computed on M_2 grid ($Q^W_{M_2}$) (see Fig. 21b, c). On the finest grid M_5 the differences are less, but still significant, as the extrapolated value of the resolved variance ($Q^W_\circ \approx 0.04$) is approximately 26% higher than that on M_5 grid ($Q^W_{M_5} \approx 0.0317$) at the location of $x/D = 7.5$, $r/D = 0.65$ and 23% higher ($Q^W_{M_5} \approx 0.0325$) at the location of $x/D = 15$,

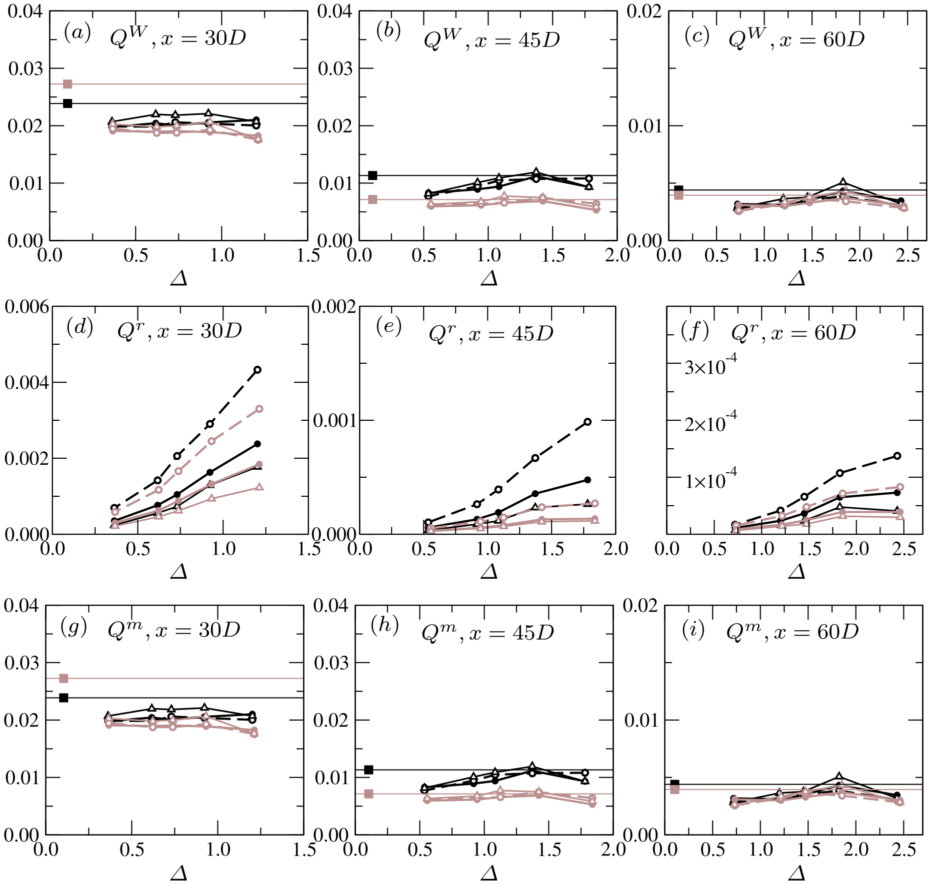

Fig. 22 Convergence of the mixture fraction variances: $Q^W(\Delta)$, $Q^r(\Delta)$ and $Q^m(\Delta)$ at the axial and two radial locations—closer to (*dark lines*) and farther from (*light lines*) the centerline: (**a**, **d**) $x = 30D$, $r_1 = 0.9D$, $r_2 = 1.4D$; (**b**, **e**) $x = 45D$, $r_1 = 1.5D$, $r_2 = 3D$; (**c**, **f**) $x = 60D$, $r_1 = 2D$, $r_2 = 3D$, and for: DSMG (△), Vreman-I (●), Vreman-II (○) and experiment (■). Each point (from *right* to *left*) corresponds to grids $M_1 - M_5$. The experimental values correspond to the resolution $\Delta^S_{\text{exp}} = 0.104D$

$r/D = 0.7$, respectively. At the fuel-lean locations the resolved variance appears to be more converged as the corresponding profiles are more flat as can be seen from Figs. 21a–c and 22a–c. At the downstream location of $x/D = 30$ the resolved mixture fraction variance depends on Δ very weakly and is approximately converged. As the resolution scale grows downstream, due to the grid stretching, $Q^W(\Delta)$ starts to exhibit some considerable dependence on Δ as shown in Fig. 22c for $x/D = 60$. Here, the extrapolated value of the resolved variance $Q^W_\circ$ is about 28% and 50% less than that on M_5 and M_2 grids, respectively. Note, however, that the corresponding mixture fraction rms $\tilde{\xi}^{\text{rms}}_\circ = \sqrt{Q^W_\circ}$ would demonstrate significantly weaker dependence on Δ with the value ($\tilde{\xi}^{\text{rms}}_\circ \approx 0.0444$) which is about 15% ($\tilde{\xi}^{\text{rms}}_{M_5} \approx 0.0525$) and 28% ($\tilde{\xi}^{\text{rms}}_{M_2} \approx 0.0624$) less than the values computed on M_2 and M_5 grids, respectively. It is interesting to note that the dependence on an SGS model is minimal. Both

Vreman models produce essentially the same results that are independent of the model constant C_v suggesting that a role of the SGS model is of minor importance and the results are strongly dominated by numerics.

The Δ-dependence of the mean SGS variance Q^r is shown in Figs. 21d–f and 22d–f. While the mean SGS variance generally decreases with Δ, as expected, its functional dependence on Δ is complicated. In the near-field, for axial locations of $x/D = 3$ and 7.5, Q^r decreases in approximately linear fashion on the four finest grids $M_2 - M_5$, but farther downstream at axial locations of $x/D \geq 15$ the dependence appears to be weakly quadratic as it is evident from Figs. 21f and 22d–f. This suggests that there is no universal scaling and the Δ-dependence for the mean SGS variance can be generally expressed as $Q^r(\Delta) = a\Delta^p$, with a and p being some functions of spatial coordinates. The mean SGS variance is quite significant at the upstream locations and is at least about 15% (on the finest grid M_5), or more, of the corresponding resolved variance value at $x/D = 3$. On the other hand, Q^r rapidly decreases downstream and becomes an order of magnitude smaller that the resolved variance starting from $x/D = 30$. This indicates that even if there are regions where the Δ-dependence of Q^r deviates from a linear functional form they might not contribute significantly to the total mixture fraction variance Q^m.

Figures 21d–f and 22d–f demonstrate that the mean SGS variance strongly depends on the Vreman model constant C_v (for Vreman SGS models). In particular, Q^r for the Vreman-II SGS model is significantly larger than Q^r for the Vreman-I SGS model for all axial locations considered, i.e., $Q^r_{II} > Q^r_I$. Such behavior can be qualitatively understood from a governing equation for the SGS variance (Eq. 4). Note that after the substitution of a model for the scalar dissipation rate (Eq. 5) into Eq. 4 it becomes an equation of the advection-diffusion type where the forcing term $2\bar{\rho}\mathcal{D}_T(V_\xi/\Delta^2 - |\nabla\xi|^2)$ is subtracted on the right hand side. The larger positive forcing term would provide more dissipative action and tend to decrease the SGS variance. On the other hand, the negative forcing term would act as the source term and promote higher values of the SGS variance. Since the subgrid diffusivity ($\mathcal{D}_T \geq 0$) is proportional to the Vreman constant it assumes higher values for Vreman-II SGS model. Thus, the higher values of Q^r_{II} in the near-field can be related to the negative forcing term due to high values of the scalar gradient (i.e., $V_\xi/\Delta^2 < |\nabla\xi|^2$). Farther downstream (for $x/D > 15$), as the scalar gradient becomes weak and Δ continues increasing in magnitude the difference $(V_\xi/\Delta^2 - |\nabla\xi|^2)$ appears to retain its sign, thus leading to $Q^r_{II} > Q^r_I$.

5 Conclusions

The sensitivity of LES statistics to the turbulence resolution scale Δ and to different SGS models has been studied for the piloted non-premixed Sandia flame D. Five grids $(M_1 - M_5)$ with progressively increasing resolution from 0.3 to about 10.4 million cells have been employed to generate the LES statistics. A steady laminar flamelet combustion model has been adopted to parameterize reacting density and temperature in terms of the mixture fraction and its subgrid variance based on a flamelet CHEMKIN simulation with a detailed chemistry mechanism.

The dependence of the LES statistics on the turbulence resolution scale Δ has been analyzed for two eddy-viscosity based SGS models—the standard dynamic Smagorinsky model and the Vreman SGS model [22]. As the representative LES statistics of interest, the mean and rms of the streamwise velocity as well as the mean and variances of the mixture fraction have been chosen, respectively. In addition, the effect of the Vreman model constant on the convergence of the LES statistics has been studied to assess a potential need for a procedure allowing a dynamic determination of the constant, by considering two cases—one with the standard value of the Vreman constant and the other where the value is twice as large.

The results obtained demonstrate that all models perform well and reproduce the essential features of the Sandia flame D satisfactorily. The Vreman model is found to be capable of producing the LES statistics that are negligibly different from that of the dynamic Smagorinsky model. This makes it a preferable choice in practical LES of similar type of flows taking into account the inherent absence of the ad-hoc procedures such as clipping and averaging. Furthermore, it was found that the effect of the model constant on the the resolved variance and mean of both velocity and mixture fraction fields is minimal. On the other hand, the mean SGS variance is strongly affected by a choice of the model constant in the jet near-field where the larger constant value leads to the higher levels of the SGS variance. This suggests, however, that a choice of the model constant might have stronger effects in flame configurations which are more sensitive to the modeling of the SGS variance such as lifted flames. Overall, the Δ-dependence of the mean and resolved variance shows that the results are rather insensitive to SGS modeling and mostly influenced by numerics.

The mean velocity field has been found convergent with respect to Δ throughout most of the domain on the four finest grids, while the mean mixture fraction has been shown to be sensitive to Δ and to have an approximate linear dependence on Δ for these grids. The rms of velocity is characterized by the weak and approximately linear dependence on Δ for $M_2 - M_5$ grids which is the highest in the near-field. Similarly, the resolved mixture fraction variance exhibits strong dependence on Δ in the near-field and on the fuel-rich side of the jet which gradually decreases upstream and becomes linear.

In summary, the results obtained show that the convergence of the LES statistics may differ significantly depending on the type of the statistics and the considered flow variables. Moreover, this convergence may not be uniform in space even for a particular statistic type and a particular flow variable which makes the results obtained on one LES grid, or even on several grids, potentially susceptible to high levels of uncertainty. This, therefore, necessitates a procedure which allows one to remove the Δ-dependence from the LES statistics, for example, through a limiting process to the DNS limit, to be an essential part of an LES study.

Acknowledgements This work was supported by the Air Force Office of Scientific Research (AFOSR) under Grant No. FA-9550-09-1-0047 and by Grant No. FA-9550-09-1-0611 funded by AFOSR and NASA ARMD, technical monitors Julian Tishkoff (AFOSR) and Aaron Auslender and Rick Gaffney (NASA). This research was also supported in part by the National Science Foundation through TeraGrid resources provided by National Institute for Computational Science (NICS) under Grant No. TG-CTS090020.

References

1. Pitsch, H.: Large-eddy simulation of turbulent combustion. Annu. Rev. Fluid Mech. **38**, 453 (2006)
2. Guermond, J.L., Oden, J.T., Prudhomme, S.: Mathematical perspective on large eddy simulation models for turbulent flows. J. Math. Fluid Mech. **6**, 195 (2004)
3. di Mare, F., Jones, W.P., Menzies, K.R.: Large eddy simulation of a model gas turbine combustor. Combust. Flame **137**, 278 (2004)
4. Mahesh, K., Constantinescu, G., Apte, S., Iaccarion, G., Ham, F., Moin, P.: Large-eddy simulation of reacting turbulent flows in complex geometries. J. Appl. Mech. **73**, 374 (2006)
5. Boileau, M., Staffelbach, G., Cuenot, B., Poinsot, T., Bérat, C.: LES of an ignition sequence in a gas turbine engine. Combust. Flame **154**, 2 (2008)
6. Patel, N., Menon, S.: Simulation of spray-turbulence-flame interactions in a lean direct injection combustor. Combust. Flame **153**, 228 (2008)
7. Boudier, G., Gicquel, L.Y.M., Poinsot, T.J.: Effects of mesh resolution on large eddy simulation of reacting flows in complex geometry combustor. Combustion and Flame **155**, 196 (2008)
8. Celik, I., Klein, M., Janicka, J.: Assessment measures for engineering LES applications. J. Fluids Eng. **131**, 031102 (2009)
9. Vreman, B., Geurts, B.J., Kuerten, H.: Comparison of numerical schemes in large-eddy simulations of the temporal mixing layer. Int. J. Numer. Methods Fluids **22**, 297 (1996)
10. Geurts, B.J., Fröhlich, J.: A framework for predicting accuracy limitations in large-eddy simulation. Phys. Fluids **14**, L41 (2002)
11. Meyers, J., Geurts, B.J., Baelmans, M.: Database analysis of errors in large-eddy simulation. Phys. Fluids **15**, 2740 (2003)
12. Meyers, J., Geurts, B.J., Sagaut, P.: A computational error -assessment of central finite-volume discretizations in large-eddy simulation using a Smagorinsky model. J. Comput. Phys. **227**, 156 (2007)
13. Geurts, B.J.: Analysis of errors occurring in large eddy simulation. Phil. Tran. R. Soc. A **367**, 2873 (2009)
14. Pope, S.B.: Ten questions concerning the large-eddy simulations of turbulent flows. New J. Phys. **6**, 35 (2004)
15. Pope, S.B.: Self-conditioned fields for large-eddy simulations of turbulent flows. J. Fluid Mech. **652**, 139 (2010)
16. Klein, M.: An attempt to assess the quality of large eddy simulations in the context of implicit filtering. Flow Turbul. Combust. **75**, 131 (2005)
17. Celik, I.B., Cehreli, Z.N., Yavuz, I.: Index of resolution quality for large eddy simulations. J. Fluids Eng. **127**, 949 (2005)
18. Gant, S.E.: Reliability issues of LES-related approaches in an industrial context. Flow Turbul. Combust. **84**, 325 (2010)
19. Bose, S.T., Moin, P., You, D.: Grid-independent large-eddy simulation using explicit filtering. Phys. Fluids **22**, 105103 (2010)
20. Nik, M.B., Yilmaz, S.L., Sheikhi, M.R.H., Givi, P.: Grid resolution effects on VSFMDF/LES. Flow Turbul. Combust. **85**, 677 (2010)
21. Germano, M., Piomelli, U., Moin, P., Cabot, W.H.: A dynamic subgrid-scale eddy viscosity model. Phys. Fluids A **3**, 1760 (1991)
22. Vreman, A.W.: An eddy-viscosity subgrid-scale model for turbulent shear flow: algebraic theory and applications. Phys. Fluids **16**, 3670 (2004)
23. Barlow, R.S., Frank, J.H.: Effects of turbulence on species mass fractions in methane/air jet flames. Proc. Combust. Inst. **27**, 1087 (1998)
24. Schneider, C., Dreizler, A., Janicka, J., Hassel, E.P.: Flow field measurements of stable and locally extinguishing hydrocarbon-fuelled jet flames. Combust. Flame **135**, 185 (2003)
25. Pitsch, H., Steiner, H.: Large-eddy simulation of a turbulent piloted methane/air diffusion flame (Sandia flame D). Phys. Fluids **12**, 2541 (2000)
26. Kempf, A., Flemming, F., Janicka, J.: Investigation of lengthscales, scalar dissipation, and flame orientation in a piloted diffusion flame by LES. Proc. Combust. Inst. **30**, 557 (2005)
27. Sheikhi, M.R.H., Drozda, T.G., Givi, P., Jaberi, F.A., Pope, S.B.: Large eddy simulation of a turbulent nonpremixed piloted methane jet flame (Sandia flame D). Proc. Combust. Inst. **30**, 549 (2005)

28. Raman, V., Pitsch, H.: A consistent LES/filtered-density function formulation for the simulation of turbulent flames with detailed chemistry. Proc. Combust. Inst. **31**, 1711 (2007)
29. Ihme, M., Pitsch, H.: Prediction of extinction and reignition in nonpremixed turbulent flames using a flamelet/progress variable model 2. Application in LES of Sandia flames D and E. Combust. Flame **155**, 90 (2008)
30. Vreman, A.W., Albrecht, B.A., van Oijen, J.A., de Goey, L.P.H., Bastiaans, R.J.M.: Premixed and nonpremixed manifolds in large-eddy simulation of Sandia flame D and F. Combust. Flame **153**, 394 (2008)
31. Clayton, D.J., Jones, W.P.: Large eddy simulation of methane-air diffusion flame. Flow Turbul. Combust. **81**, 497 (2008)
32. Kemenov, K.A., Pope, S.B.: Molecular diffusion effects in LES of a piloted methane-air flame. Combust. Flame **158**, 240 (2011)
33. Peters, N.: Laminar diffusion flamelet models in non-premixed turbulent combustion. Prog. Energy Combust. Sci. **10**, 319 (1984)
34. Branley, N., Jones, W.P.: Large eddy simulation of a turbulent non-premixed flame. Combust. Flame **127**, 1914 (2001)
35. Pierce, C.D., Moin, P.: Progress-variable approach for large-eddy simulations of non-premixed turbulent combustion. J. Fluid Mech. **504**, 73 (2004)
36. Cook, A.W., Riley, J.J.: A subgrid model for equilibrium chemistry in turbulent flows. Phys. Fluids **6**, 2868 (1994)
37. Domingo, P., Vervisch, L., Veynante, D.: Large eddy simulation of a lifted jet flame in a vitiated coflow. Combust. Flame **152**, 415 (2008)
38. Lilly, D.K.: A proposed modification of the Germano subgrid-scale closure method. Phys. Fluids A **4**, 633 (1992)
39. Choi, J., Tawhai, M.H., Hoffman, E.A., Lin, C.L.: On intra- and intersubject variabilities of airflow in the human lungs. Phys. Fluids **21**, 101901 (2009)
40. Park, N., Lee, S., Lee, J., Choi, H.: A dynamic subgrid-scale eddy viscosity model with a global model coefficient. Phys. Fluids **18**, 125109 (2006)
41. Leonard, B.P.: Comput. A stable and accurate convective modeling procedure based on quadratic upstream interpolation. Methods Appl. Math. Eng. **19**, 59 (1979)
42. Vervisch, L., Domingo, P., Lodato, G., Veynante, D.: Scalar energy fluctuations in large-eddy simulation of turbulent flames: statistical budget and mesh quality criterion. Combust. Flame **157**, 778 (2010)
43. Pera, C., Réveillon, J., Vervisch, L., Domingo, P.: Modeling subgrid scale mixture fraction variance in LES of evaporating spray. Combust. Flame **146**, 635 (2006)